

Hydraulic transport through calcite bearing faults with customized roughness: Effects of normal and shear loading.

Mateo Acosta¹, Marie Violay¹, and Robin Maye²

¹EPFL

²KFSA

November 26, 2022

Abstract

Understanding fluid flow in rough fractures is of high importance to large scale geologic processes and to most anthropogenic geo-energy activities. Here, we conducted fluid transport experiments on Carrara marble fractures with a novel customized surface topography. Transmissivity measurements were conducted under mechanical loading conditions representative of deep geothermal reservoirs (normal stresses from 20 to 70 MPa and shear stresses from 0 to 30 MPa). A numerical procedure simulating normal contact and fluid flow through fractures with complex geometries was validated towards experiments. Using it, we isolated the effects of roughness parameters on fracture fluid flow. Under normal loading, we find that i) the transmissivity decreases with normal loading and is strongly dependent on fault geometry ii) the standard deviation of heights (RMS) and macroscopic wavelength of the surface asperities control fracture transmissivity. Transmissivity evolution is non-monotonic, with more than 4 orders of magnitude difference for small variations of macroscopic wavelength and RMS roughness. Reversible shear loading has little effect on transmissivity, it can increase or decrease depending on the combined contact geometry and overall stress state on the fault. Finally, irreversible shear displacement (up to 1 mm offset) slightly decreases transmissivity contrary to common thinking. The transmissivity variation with irreversible shear displacements can be predicted geometrically at low normal stress only. Finally, irreversible changes in surface roughness (plasticity and wear) due to shear displacement result in a permanent decrease of transmissivity when decreasing differential stress. We discuss the implications for Enhanced Geothermal Systems stimulation.

15 **Abstract**

16 Understanding fluid flow in rough fractures is of high importance to large scale geologic
17 processes and to most anthropogenic geo-energy activities. Here, we conducted fluid transport
18 experiments on Carrara marble fractures with a novel customized surface topography.
19 Transmissivity measurements were conducted under mechanical loading conditions
20 representative of deep geothermal reservoirs (normal stresses from 20 to 70 MPa and shear
21 stresses from 0 to 30 MPa). A numerical procedure simulating normal contact and fluid flow
22 through fractures with complex geometries was validated towards experiments. Using it, we
23 isolated the effects of roughness parameters on fracture fluid flow. Under normal loading, we
24 find that i) the transmissivity decreases with normal loading and is strongly dependent on fault
25 geometry ii) the standard deviation of heights (RMS) and macroscopic wavelength of the surface
26 asperities control fracture transmissivity. Transmissivity evolution is non-monotonic, with more
27 than 4 orders of magnitude difference for small variations of macroscopic wavelength and RMS
28 roughness. Reversible shear loading has little effect on transmissivity, it can increase or decrease
29 depending on the combined contact geometry and overall stress state on the fault. Finally,
30 irreversible shear displacement (up to 1 mm offset) slightly decreases transmissivity contrary to
31 common thinking. The transmissivity variation with irreversible shear displacements can be
32 predicted geometrically at low normal stress only. Finally, irreversible changes in surface
33 roughness (plasticity and wear) due to shear displacement result in a permanent decrease of
34 transmissivity when decreasing differential stress. We discuss the implications for Enhanced
35 Geothermal Systems stimulation.

36 **1 Introduction**

37 Fluids are pervasive in Earth's crust. They interact with rocks, modifying their physical
38 properties and deformation mechanisms. In turn, host rocks control the way fluids migrate in the
39 crust either due to natural forcing or to anthropogenic activities (Sibson, 1994;1996). Rock
40 masses in the brittle-crust are pervasively fractured and have permeabilities ranging from around
41 10^{-16} to 10^{-17} m² (Townend and Zoback, 2000; Faulkner et al., 2010). These permeability values
42 are more than two to three orders of magnitude larger than those of the intact rock matrix (10^{-21}
43 to 10^{-19} m²) at depths ranging from ~2 to 15 km. Most of the fluid flow needs therefore to be
44 controlled by single fractures or fracture networks. Thus, it is of outmost importance to

45 understand how fractures and faults transport fluids in the subsurface. This is particularly valid
46 for the safe, and clean development of underground anthropogenic geo-energy activities such as
47 geothermal energy exploitation (Breede et al., 2013; Violay et al., 2015; 2017). Indeed, a popular
48 strategy for enhancing fluid transport in Enhanced Geothermal Systems (EGS) is fracture hydro-
49 shearing, by fluid injection. It consists on reactivating pre-existing faults to increase the deep
50 crystalline reservoir's permeability (Cladouhos et al., 2010; Breede et al., 2013). Nevertheless,
51 the enhancement of fluid flow following stimulations in such reservoirs remains poorly
52 predicted. A too low subsurface production flow rate results in economic losses while too high
53 flow rates can lead to fluid leak off and reactivation of faults located far from the injection wells.
54 This was the case of the St.Gallen geothermal project (Zbinden et al., 2020) and possibly of
55 several other injection induced seismicity cases (Ellsworth, 2013; Lengliné et al., 2014; Goebel
56 and Brodsky, 2018; Yeck et al., 2016; Kim et al., 2018; Grigoli et al., 2017). The poorly
57 estimated flow rates partly arise due to the difficulties in detecting the fracture networks in the
58 underground and partly due to the difficulties of estimating fluid flow through rough fractures
59 with complex surface topographies, submitted to large stresses. Natural rock fractures show self-
60 similar roughness properties (Brown and Scholz, 1985; Power et al., 1987; Brown, 1987;
61 Candela et al., 2009; 2012; Renard et al., 2013) at all scales. In addition, exhumed fault walls
62 often show grooves parallel to the main slip direction (Petit, 1987; Means, 1987; Power et al.,
63 1987; Power and Tullis, 1989; Engelder and Scholz, 1976; Toy et al., 2017). These features
64 result in surfaces with high elevation zones (peaks) and low elevation zones (or valleys). Several
65 methods exist for quantifying the statistical properties of rough surfaces (Brown and Scholz,
66 1985; Grasselli and Eger, 2003; Candela et al., 2009; 2012; Renard et al., 2013; Jacobs et al.,
67 2017; Yastrebov et al., 2017). As two fracture surfaces come in contact they form a three-
68 dimensional distribution of local contacts (asperities) and voids (apertures) which in turn
69 determine how fluids can circulate through the fracture.

70 The geometrical aperture distribution is strongly dependent on the contact geometry and on the
71 stress applied on the fracture because they both affect the equivalent hydraulic aperture, through
72 which fluids can flow (Zimmerman and Bodvarsson, 1996). Complex contact geometries can
73 also lead to flow channeling in fractures (Watanabe et al., 2009; Kang et al., 2016) drastically
74 affecting their hydraulic transport capacity. Most experimental works have been performed either
75 at low stresses (Patir and Cheng, 1978; Witherspoon et al., 1980; Park and Song, 2013;

76 Tanikawa et al., 2010; Wenning et al., 2019), or on faults with constant roughness (Watanabe et
77 al., 2008; Faoro et al., 2009; Rutter and Mecklenburgh, 2017; 2018).

78 The application of normal stress has been shown to increase the real contact area between the
79 two fracture walls, and to reduce the geometrical aperture and hydraulic transmissivity
80 (Witherspoon et al., 1980; Walsh, 1981; Renshaw, 1995; Brown 1987; Brown et al., 1998;
81 Pyrak-Nolte and Morris, 2000; Watanabe et al., 2008; 2009; Kang et al., 2016; Rutter and
82 Mecklenburgh, 2017; 2018). After passing a stress value (percolation threshold) the fracture
83 reaches a configuration where further increases in normal stress result in small changes in the
84 hydraulic aperture. Then, fracture transmissivity remains constant due to the formation of
85 preferential channels in between the highly stressed asperities (Brown et al., 1998; Pyrak-Nolte
86 et al., 1988; Durham, 1997; Watanabe et al., 2008; 2009; Kang et al., 2016). The influence of
87 reversible shear loads (in the elastic domain) has been rarely studied experimentally. In some
88 few observations, it is seen that reversible shear loading (elastic loading, with no displacement)
89 can cause a slight decrease in fracture transmissivity (in relatively smooth fractures of hard rock;
90 Faoro et al., 2009; Rutter and Mecklenburgh, 2017; 2018). Most of the effort has been put to
91 determine the effect of irreversible shear displacement on fracture transmissivity, usually
92 considering large displacements (more than 1-20 millimeters) at low stresses (usually lower than
93 20 MPa), and/or on rock fractures generated by tensile or shear fracturing as well as on artificial
94 rock proxies (Carey et al., 2015; Ishibashi et al., 2012; Lee and Cho, 2002; Yeo et al., 1998;
95 Zambrano et al., 2018; Pyrak-Nolte et al., 1988; Olsson and Brown, 1993; Esaki et al., 1999;
96 Wenning et al., 2019; Chen et al., 2000; Watanabe et al., 2008; 2009). From such studies, the
97 usual knowledge with respect to the influence of shear displacement on transmissivity is that it
98 strongly increases hydraulic transport on the fault. In contrast, recent studies (Rutter and
99 Mecklenburgh, 2017; 2018) have shown that for displacements inferior to 1 mm, on real rock
100 samples with smooth surfaces, at high stresses (up to 100 MPa normal stress) the transmissivity
101 rather decreases or remains fairly constant with increasing shear displacement. These types of
102 studies seem more relevant to fault reactivation due to anthropogenic activities (in EGS
103 stimulation for example) particularly because the reactivation of reservoir faults needs to target
104 small displacements to avoid large magnitude seismicity.

105 In this work, we developed an experimental technique to customize the roughness of hard-rock
106 fracture surfaces by imposing different macroscopic wavelengths in sub-orthogonal and sub-

107 parallel directions with respect to the sense of fluid flow. Then, the fluid flow through the wavy-
108 rough fractures was experimentally measured both under normal loading only (up to 40 MPa)
109 and under reversible shear loading (up to shear and normal stresses close to 30 and 80 MPa
110 respectively). The fractures loaded in shear were then submitted to irreversible shear
111 displacement (up to 1 mm total offset). A numerical procedure that first simulates the normal
112 contact between wavy-rough surfaces and then fluid flow through them was developed and
113 verified with the experimental results. It is noteworthy that the numerical procedure consists on a
114 combination of open-source models. Through the use of the calibrated numerical procedure, we
115 isolated the effects of roughness parameters on fracture transmissivity under normal load. The
116 numerical procedure was also used to isolate the influence of reversible shear loads on
117 transmissivity. Finally, we evaluated how the small transmissivity changes during irreversible
118 shear displacement can be predicted by a change in geometry of the fracture surface for different
119 applied normal stresses.

120 **2. Experimental materials and methods.**

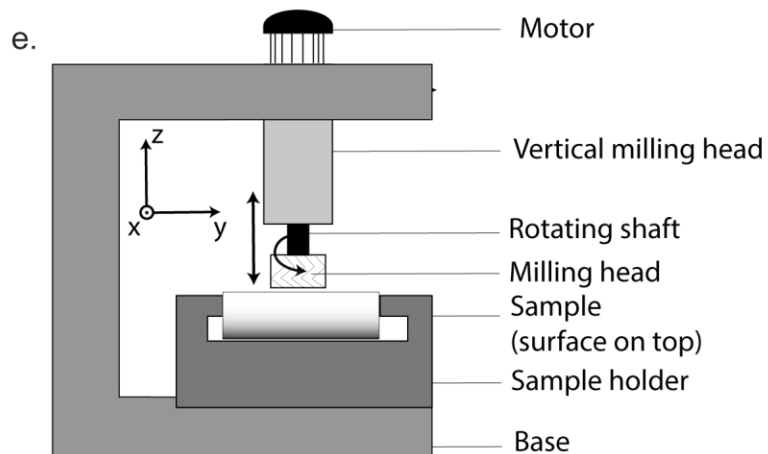
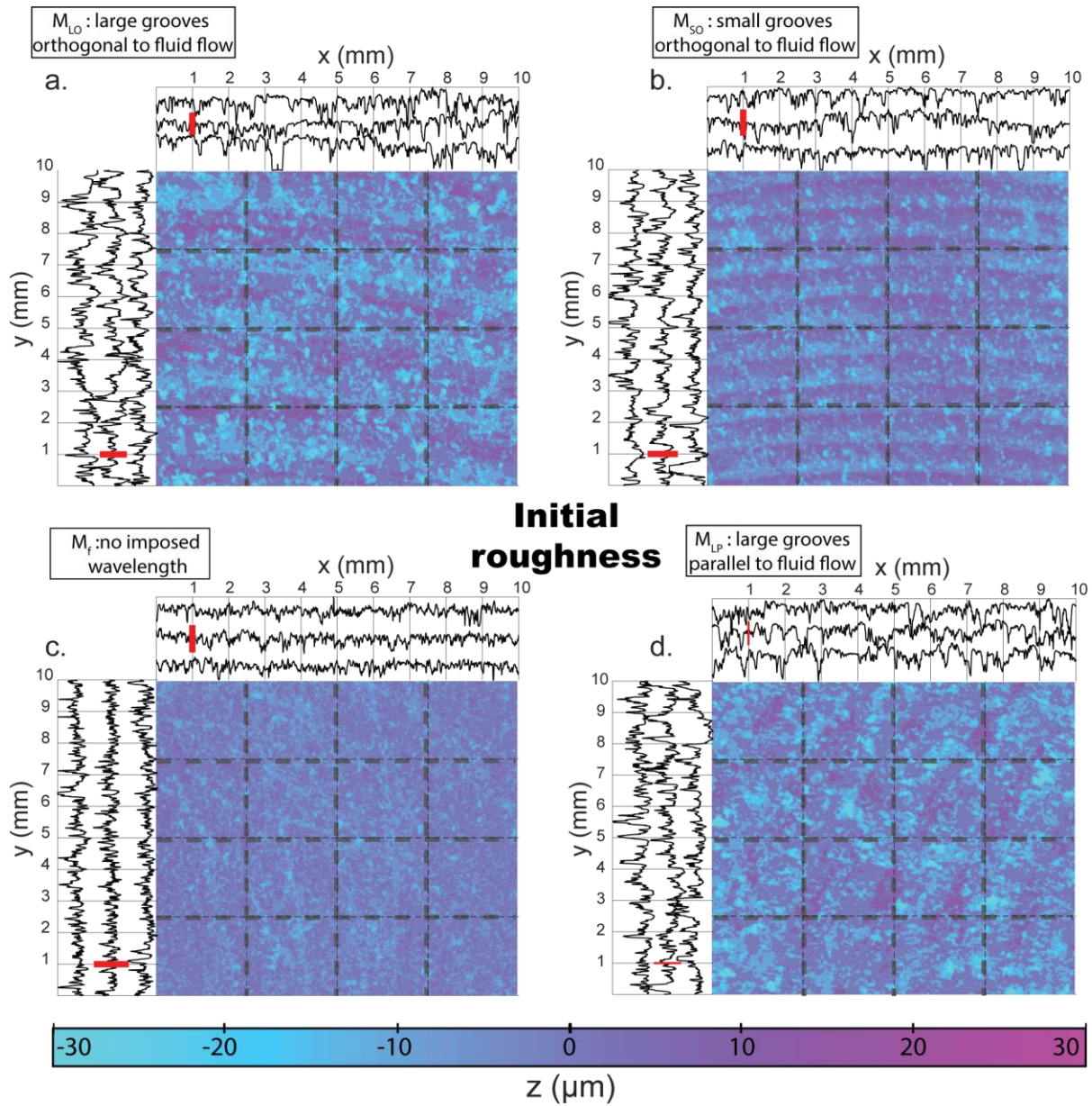
121 2.1 Starting samples with customized roughness.

122 The samples were 75 mm long cylinders (36 mm diameter) of Carrara marble. Carrara marble
123 has a well characterized mineralogy (~99 vol% calcite), low porosity (~1%), fine grain (average
124 grain size <0.5 mm), and high homogeneity and isotropy (Chen, 1995; Pieri et al., 2001; Delle-
125 Piane et al., 2015). Its mechanical properties (Young's modulus ~30 GPa and uniaxial
126 compressive strength ~160 GPa; Edmond and Paterson 1972; Paterson and Wong, 2005) make it
127 a standard in rock mechanics and an ideal material for laboratory testing. For normal loading
128 experiments, two semi-cylinder's vertical flat faces were ground prior to sample coring, to obtain
129 a perfect semi-circular geometry. For shear loading and reactivation experiments, the cylinders
130 were cored first, and then saw-cut at 30° towards the cylinder's long axis to create an oriented
131 fracture. The fracture's faces were ground flat to ensure perfect contact. Finally, an
132 injection/extraction borehole of 2 mm diameter was drilled in each half sample from the
133 horizontal flat surface (in contact with the top/bottom anvils) to inject/extract fluid directly
134 into/from the fracture. In saw cut configuration, the resulting fracture was of elliptical shape with
135 long axis $2a_e = 72 \text{ mm}$ and short axis $2b_e = 36 \text{ mm}$. The elliptical contacting fracture surfaces

136 had a nominal area $A \sim 2036 \text{ mm}^2$. Prior to loading, the distance between boreholes centers was
137 of 60 mm.

138 For all experiments, a customized fracture roughness was imposed to each flat surface of the
139 half-samples using a vertical-axis milling machine. The machine (Figure 1e) is composed of
140 three main elements: i) A table where the half samples were locked and leveled to a horizontal
141 position. ii) A rotary milling cutter mechanically linked to a rotating spindle whose spin is
142 controlled by a motor. The rotary cutter can be lowered to enter in slight contact with the half
143 sample iii) An automatically advancing arm mechanically fixed to the rotary cutting tool. As the
144 rotary cutting tool advances, it periodically removes rock material over the tool blade's edge,
145 making arc shaped grooves on the sample's surface. The grooves' wavelengths are smaller for
146 faster advancement speeds and larger for slower ones, resulting in customized roughness
147 depending on the advancement speeds.

148 The different experimental geometries are detailed in Table 1 and shown in Figure 1a-d. In the
149 sample's names, the first subscript denotes large or small macroscopic wavelength (L or S) and
150 the second subscript denotes the sense of fluid flow with respect to the macroscopic grooves (P
151 for sub-parallel and O for sub-orthogonal). Finally M_f denotes the sample with no imposed
152 macroscopic wavelength where the roughness was manually imposed through #80 grit. In all
153 experiments, fluid flow occurred following the y-axis (fracture's long axis) as defined in Figure
154 1. In experiments with shear loading and displacement, shear occurred along the y-axis.



156

157 Figure 1: Customized initial fracture roughness. a-d. Roughness measurements of the four types
158 of experimental samples. Colorbar represents the measured heights over the area. The transects
159 in x-axis and y-axis in dotted lines are presented in the top and left plots respectively. For
160 reference, a red bar represents 30 micrometers height. a. Sample M_{LO} , large wavelength with
161 grooves sub-orthogonal to fluid flow and shear direction. b. Sample M_{SO} , small wavelength with
162 grooves sub-orthogonal to fluid flow and shear direction. c. Sample M_f , no imposed macroscopic
163 wavelength. d. Sample M_{LP} , large wavelength with grooves ‘sub-parallel’ to fluid flow and shear
164 direction. d. Diagram of the milling apparatus. Displacement rate over the y-axis can be
165 controlled. The x-axis is fixed. Movement over the z-axis can be changed and fixed at a given
166 position (0.1 mm under the sample’s surface).

167 2.2 Roughness measurement and data processing.

168 The measurement of surface roughness was performed using a 3D optical profilometer (Contour
169 GT-I 3D Optical Microscope by Bruker Nano surfaces Division). The tool uses green light
170 interferometry to determine the surface topography of the sample with an accuracy down to ~100
171 nm. The green light pulse has an area of ~1 mm². A motorized base allows sample movement in
172 the x and y directions (minor and major axis of the fracture respectively). The tool allows
173 automatic scanning of large surfaces by performing several measurements with a given overlap
174 (here of 20%) which are later stitched together to reconstruct a larger surface topography.
175 Under this configuration, two overlapping areas of sample M_{LO} were analyzed. The first area had
176 a surface of 1 cm*1 cm and the second area had a 3 cm * 3 cm area. The measurement results
177 showed that the surfaces’ statistical properties (radially averaged 2-Dimensional PSD) are
178 transitionally invariant. Hence, it is assumed that taking only a portion of 1 cm² of the sample’s
179 surface instead of taking the whole area gives statistically the same result. Thus, for time
180 purposes, only an area of 1 cm² was analyzed on the profilometer for all other samples.
181 The following corrections were then applied to the measured data (x,y,z profiles): i) Tilt
182 removal. The intrinsic tilt due to levelling error at measurement was removed. ii) Interpolation of
183 missing points. Missing values are a specific consequence of rough surface because the reflected
184 light path can be cut when large slopes are encountered (Jacobs et al., 2017). A 2D nearest

185 neighbor interpolation technique (Pingel et al., 2013) was used in order to interpolate the missing
186 data points. iii) Correction for sampling artifacts. The sampling theorem states that the minimum
187 wavenumber to be considered in spectral analysis should be smaller than the Nyquist frequency
188 $f_N = \frac{N}{2L}$ where N is the total number of points in the sampled domain (N= 5044) and L=10 mm
189 is the length of the measured domain. Thus, the cut-off wavenumber (e.g the maximum wavenumber
190 analysed) should be $q_{cut} = 2.5e5 \text{ m}^{-1}$. A low-pass Gaussian filter was applied to remove all
191 wavenumbers higher than q_{cut} in the data. Finally, to evaluate the properties of rough surfaces
192 (Figure 7), a radially averaged 2D Power Spectral Density analysis with radially symmetric
193 Welch windows was performed to avoid artifacts (PSD, Jacobs et al., 2017; Kanafi, 2019).
194 It is important to notice that in the rest of the manuscript the roughness parameters are evaluated
195 with the available data. For example, the Hurst exponent is evaluated on windows smaller than
196 one order of magnitude thus leading to an intrinsic error related to the availability of the data
197 (more data could be obtained through higher/lower resolution measurements to complement the
198 dataset). Similar difficulties arise on the estimation of the roll-off wavenumber for the
199 experimental samples. Notwithstanding the estimated intrinsic errors, the same technique was
200 applied for all the measured samples. Thus, the comparative analysis presented remains robust
201 even though the absolute values of these parameters might not be as accurate as desired.

202 2.3. Experimental set-ups and flow through experiments.

203 The experimental set up was an oil-medium tri-axial Hoek-cell (Figure 2) of the Laboratory of
204 Experimental Rock Mechanics (LEMUR) at EPFL, Switzerland. The cell can hold 70 MPa (+- 50
205 kPa resolution) in confinement pressure ($\sigma_3 = \sigma_2$). For flow through experiments, the top and
206 bottom anvils were specifically designed to allow controlled fluid pressures and volumes
207 independently at the top and bottom ends of the samples (Figure 2). The pressure/volume
208 controllers have a capacity of 200 cm³ (+-1mm³ resolution) in volume and 30 MPa (+- 10 kPa
209 resolution) in pressure.

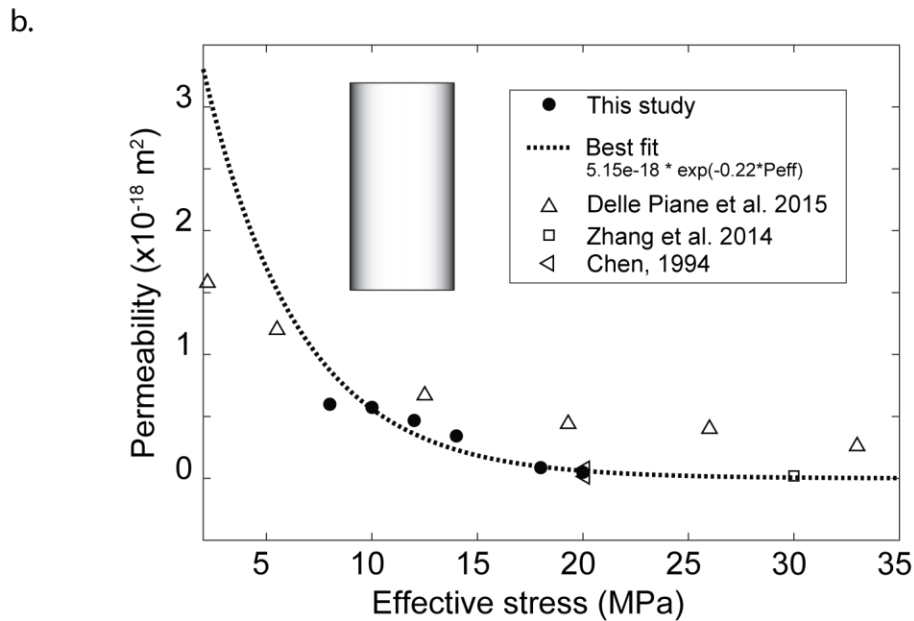
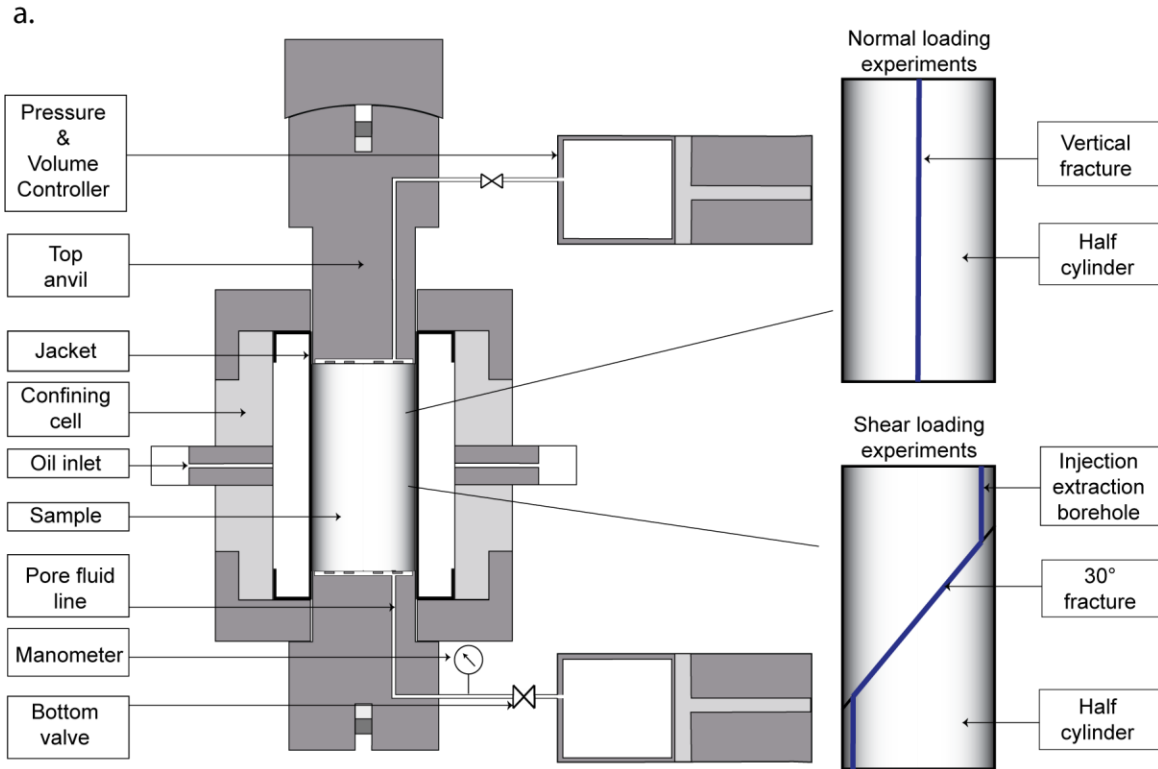
210 One experiment was performed to evaluate the matrix permeability of Carrara marble and have a
211 point of comparison for the fracture fluid flow experiments. Due to the low permeability of the
212 rock matrix, an oscillatory fluid flow method was used under the same experimental set-up.

213 Details of the oscillatory fluid flow method can be found in Bernabé et al. (2006) and Acosta and
214 Violay (2020). Matrix permeabilities ranged from $\sim 5.99 \text{ e-}19 \text{ m}^2$ at $\sigma_3' = 8 \text{ MPa}$ to $4.92 \text{ e-}20 \text{ m}^2$ at

215 $\sigma_3'=20$ MPa (Figure 2b) and the exponential decay seems consistent with previous literature
216 studies of the permeability of Carrara marble (Chen, 1994; Zhang et al., 2014; Delle-Piane et al.,
217 2015).

218

219



220

221 Figure 2. Experimental set-up and flow through experiments. a. The Hoek-cell tri-axial set-up

222 with customized fluid pressure system for flow through experiments (After Noel et al., 2019).

223 Two types of sample geometries were used for different experiment types (under normal and

224 shear loading). b. Permeability of intact Carrara marble cylinder function of effective stress.

225 Black dots represent the experimentally measured values. Empty symbols represent data from
 226 the literature. Dotted line represents the best exponential decay fit to the experimental data
 227 produced in this study.

228 Experiments under normal loading.

229 The half cylinders were clamped together and let to saturate in a vacuum chamber for a
 230 minimum of one-week. Following this, samples were confined to $\sigma_3 = 5$ MPa and fluid pressure
 231 (p_f) to 1 MPa during a minimum of 120 minutes for additional (pressurized) saturation. Once
 232 fluid and confinement pressures and volumes reached an equilibrium, σ_3 was increased to the
 233 target pressure of 43 MPa and p_f was changed stepwise to study the effect of effective normal
 234 stress ($\sigma'_N = \sigma'_3 = \sigma_3 - p_f = 28,30,32,34,36,38,40$ MPa; Figure 3a). At each step, a differential
 235 pressure $\Delta p_f = 0.3$ MPa was imposed between the top and bottom ends of the sample and the
 236 fluid flow rate (Q in $m^3 \cdot s^{-1}$) was measured (Figure 3a,b). Because the flow rate on the fracture
 237 was more than 3 orders of magnitude larger than in an intact Marble cylinder (Figure 2b), it is
 238 reasonable to assume that all the flow occurred through the fracture.

239 For each σ'_N step, the fluid flow through a fracture was quantified by the product of the
 240 permeability (k in m^2) and the effective thickness (t in m) (Rutter and Mecklenburgh; 2017;
 241 2018). kt is called the fracture's hydraulic transmissivity (kt in m^3) which can be estimated
 242 directly from Darcy's law as:

$$243 \quad kt = \frac{\mu \cdot Q}{w \cdot \frac{\Delta P}{L}}$$

244 with μ the dynamic viscosity of the fluid, w the fracture's width and L its length.

245 Experiments under shear loading.

246 The procedure to saturate the samples, place them in the cell, and take them to isostatic loading
 247 ($\sigma'_1 = \sigma'_3$) was the same as for normal loading experiments. For the shear experiments, confining
 248 pressure σ_3 was either 15 or 35 MPa and p_f was 5 or 15 MPa respectively (so that the effective
 249 confinement $\sigma'_3 = 10$ and 20 MPa). Then, the axial displacement was increased by steps of 0.1
 250 mm at a displacement rate of 10^{-6} mm.s⁻¹ Such a low displacement rate was used to allow fluid
 251 pressures equilibrium on the fault during shear loading (i.e fault drainage). Under saw-cut
 252 configuration, both shear and normal stresses on the fault increased with increase of axial
 253 displacement and were calculated as:

254
$$\tau = \frac{(\sigma'_1 - \sigma'_3)}{2} \sin(2\theta)$$

255 And

256
$$\sigma'_N = \frac{(\sigma'_1 + \sigma'_3)}{2} + \frac{(\sigma'_1 - \sigma'_3)}{2} \cos(2\theta)$$

257

258 with θ the angle between the saw-cut and the vertical.

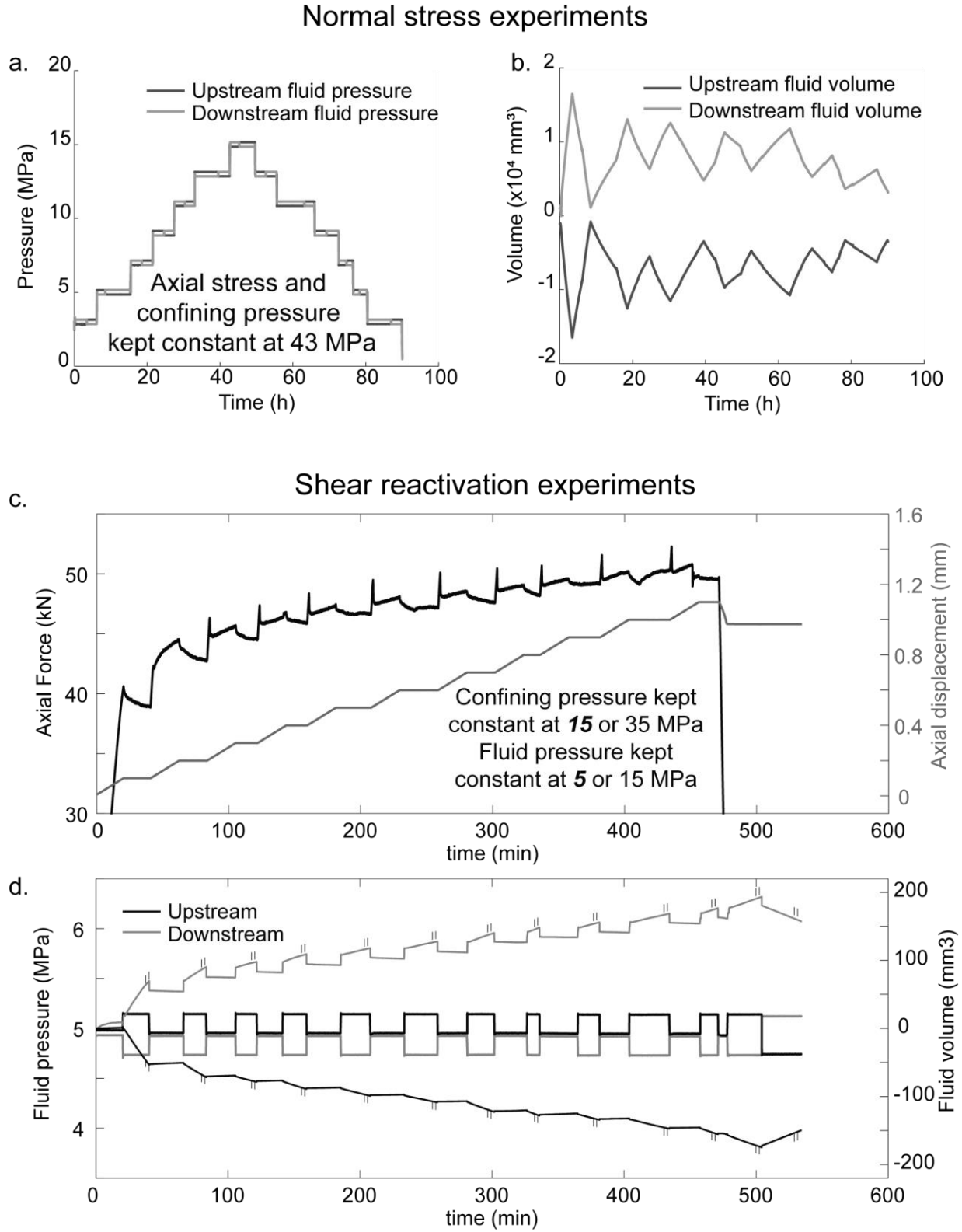
259 The final axial displacement in our experiments was of ~ 1.1 or 1.2 mm. As fault reactivation
 260 (e.g. departure from elasticity) occurred often slightly after ~ 0.1 mm displacement, the final
 261 shear offset was of ~ 1 mm in most experiments. At every displacement step, the piston's position
 262 was held constant and a differential fluid pressure of 0.3 MPa was imposed between the injection
 263 and extraction boreholes to measure sample's transmissivity (Figure 3c,d).

264 The steady state flow-rate Q was determined and the hydraulic transmissivity was estimated from
 265 the flow lines in a perfect elliptical surface using the dipole image method of Rutter and
 266 Mecklenburgh (2017; 2018) such that the transmissivity (product of permeability and equivalent
 267 hydraulic aperture) writes (Rutter and Mecklenburgh, 2017; 2018; Passelègue et al., 2020;
 268 Almakari et al., 2020):

269
$$kt = \frac{Q \cdot \mu \cdot \log_{10} \left(\frac{2a_e}{r_0} - 1 \right)}{B \cdot \pi \cdot \frac{dP}{dx}}$$

270 with a_e the half distance between the injector and extractor boreholes; r_0 the borehole diameter;
 271 $\frac{dP}{dx}$ the spatial pressure gradient between the boreholes; and B a constant close to unity (Rutter
 272 and Mecklenburgh, 2017; Passelègue et al., 2020; and Almakari et al., 2020).

273 It is noteworthy that here, no corrections for the changes in elliptical surface geometry were
 274 made (see Tembe et al., 2010) because the total displacement on the saw/cut was < 1.2 mm,
 275 resulting in a change in nominal contact area lower than 8% which would result in less than 0.5%
 276 change in transmissivity.



277

278 Figure 3. Example experiments. a,b. Normal loading experiments. Axial stress and confining
 279 pressure were fixed at 43 MPa. The changes in mean fluid pressure led to a change in effective

280 normal stress applied on the fracture. a. Upstream and downstream fluid pressures versus time. b.
 281 Upstream and downstream volumes versus time. The imposed differential pressure resulted in a
 282 symmetric volume rate at the pressure/volume controllers which was held until achieving a
 283 steady state. c,d. Shear loading experiments. c. Axial force (black) and axial displacement (grey)
 284 versus time. The increase in axial displacement led to a spontaneous evolution of the axial force
 285 (therefore of shear and normal stress) applied on the 30° saw-cut fracture. d. Fluid pressures (left
 286 x-axis) and volumes (right y-axis) versus time. A differential pressure of 0.3 MPa was imposed
 287 at every displacement step to measure transmissivity in steady state. The example in panels c and
 288 d is given for an experiment at 10 MPa effective confinement.

Experiment	Sample	Grooves ^a	σ_3	Pf	σ_3'	σ_{Nss} ^b	err σ_{Nss} ^c	τ_{ss} ^b	err τ_{ss} ^c	f_{ss} ^b	d_{ss} ^d	err d_{ss} ^e	d_{end} ^f
type	name		MPa	MPa	MPa	MPa	MPa	MPa	MPa	-	mm	mm	mm
Permeability	Intact	X	23	3:3:15	8:3:20	X	X	X	X	X	X	X	X
Normal loading	M_{LO}	⊥	43	3:2:15	28:2:40	28:2:40	X	X	X	X	X	X	X
Normal loading	M_{SO}	⊥	43	3:2:15	28:2:40	28:2:40	X	X	X	X	X	X	X
Normal loading	M_f	no	43	3:2:15	28:2:40	28:2:40	X	X	X	X	X	X	X
Normal loading	M_{LP}	∥	43	3:2:15	28:2:40	28:2:40	X	X	X	X	X	X	X
Shear loading	M_{LO}	⊥	15	5	10	37.50	2.10	15.78	1.21	0.61	0.17	0.01	1.10
Shear loading	M_{SO}	⊥	15	5	10	34.37	2.40	14.10	1.39	0.58	0.15	0.01	1.10
Shear loading	M_f	no	15	5	10	34.04	1.89	13.89	1.09	0.59	0.15	0.01	1.10
Shear loading	M_{LP}	∥	15	5	10	30.94	3.00	12.36	1.73	0.55	0.29	0.01	1.10
Shear loading	M_{LO}	⊥	35	15	20	66.30	3.60	27.01	2.08	0.58	0.26	0.01	1.17
Shear loading	M_{SO}	⊥	35	15	20	61.43	2.40	23.97	1.39	0.55	0.22	0.01	1.26
Shear loading	M_f	no	35	15	20	58.71	2.25	22.02	1.30	0.54	0.23	0.01	1.09
Shear loading	M_{LP}	∥	35	15	20	59.46	1.62	22.79	0.94	0.54	0.29	0.01	1.12

^a parallel or orthogonal to fluid flow.

^b at fault reactivation.

^c estimated from the difference between maximum and minimum during shear sliding.

^d initiation of "steady state" sliding.

^e estimated error in the determination of "steady state" sliding.

^f final axial displacement reached.

289

290

Table 1. Experiments performed and summary of mechanical results.

291

3 Numerical Methods

292

3.1. Generation of artificial surfaces.

293

Artificial wavy-rough surfaces were independently generated through use of the algorithm by

294

M.M. Kanafi (2018). The algorithm uses the roughness parameters (measured with the

295

profilometer) from the power spectral density of surface heights (h_{RMS} , H and q_r) to generate an

296

artificial randomly rough surface with the corresponding properties. In addition to the randomly

297 generated rough surface, the experimental samples had a customized macroscopic wavelength
298 (see section 2.1) which represents a singularity at a given wavevector in the radially averaged
299 PSD's (Jacobs et al., 2017). The macroscopic wavelength and the corresponding amplitude was
300 evaluated through the profilometer measurements (Table 2). The final surfaces are the resultant
301 of a random roughness created from the artificial surface generator on top of a sinusoidal
302 macroscopic wavelength estimated from the experimental samples (Figure 4a). The total
303 roughness was adjusted so that the h_{RMS} of the sum of the two surfaces is equal to the true h_{RMS}
304 measured on the experimental sample.

305 3.2. Surface contact under normal stress.

306 To simulate contact of two opposing surfaces resulting from lithostatic pressure in Geo-energy
307 reservoirs (represented by σ_3' in the experiments), a half-space based, dry contact model from
308 *Tribonet* was used (Lubrecht and Ioannides, 1991; Akchurin et al., 2015;
309 <https://www.tribonet.org/cmdownloads/tribology-simulator/>). The model uses the artificially
310 generated surfaces discretized to either 2048*682 (for model calibration) or 768*256 nodes (for
311 parametric analysis). Solid material properties were assigned to the contact bodies (which can
312 differ but are here taken equal) described by a saturating elastic stress-strain relationship (e.g. the
313 deformation is purely elastic until a stress threshold is reached, then stress remains constant with
314 increasing strain). The parameters used here are the material's Young's modulus E (here 30.2
315 GPa) and the Poisson's ratio ν (here 0.3) for elasticity (measured from a Marble deformation
316 experiment shown in Annex 1); and the yield stress σ_y (here 0.2 GPa; Violay et al., 2014) which
317 describes the limit of plasticity (or saturation threshold). The simulated load applied between the
318 half spaces corresponds to the macroscopic normal stress (here σ_3') over the nominal contact
319 area $A_n = L \cdot w$ (see Table 1 and section 2.3). The contact problem is solved under plane-
320 strain and takes into account the mechanical interactions between micro contacts (Polonsky and
321 Keer,1999) by the use of a double-continuum convolution integral. It calculates how the
322 deflection at each mesh node affects the surrounding nodes. The calculation iterates until
323 convergence of the deflection at all nodes (Lubrecht and Ioannides, 1991; Polonsky and Keer.,
324 1999; Akchurin et al., 2015; and *Tribonet*). As outputs, two-dimensional real contact area (A_r)
325 maps and geometrical aperture ($e_m(x,y)$) maps were recovered at each studied effective
326 confining pressure (Figure 4b). Note that in the aperture maps, a zero-aperture value is not

327 allowed in our procedure. Thus, the contacting zones were replaced with apertures more than ten
 328 orders of magnitude smaller than the mean aperture to avoid numerical issues for fluid flow
 329 calculation.

330 3.3. Surface contact under shear loading.

331 It is noticeable that the contact model does not include a shear stress component analysis nor a
 332 wear analysis. From our knowledge, integrating an elasto-plastic shear component and wear
 333 components to the analysis is not a straightforward task and is out of the scope of this study
 334 (Aghababaei et al., 2016; Milanese et al., 2019; Molinari et al., 2018; Frerot et al., 2019).

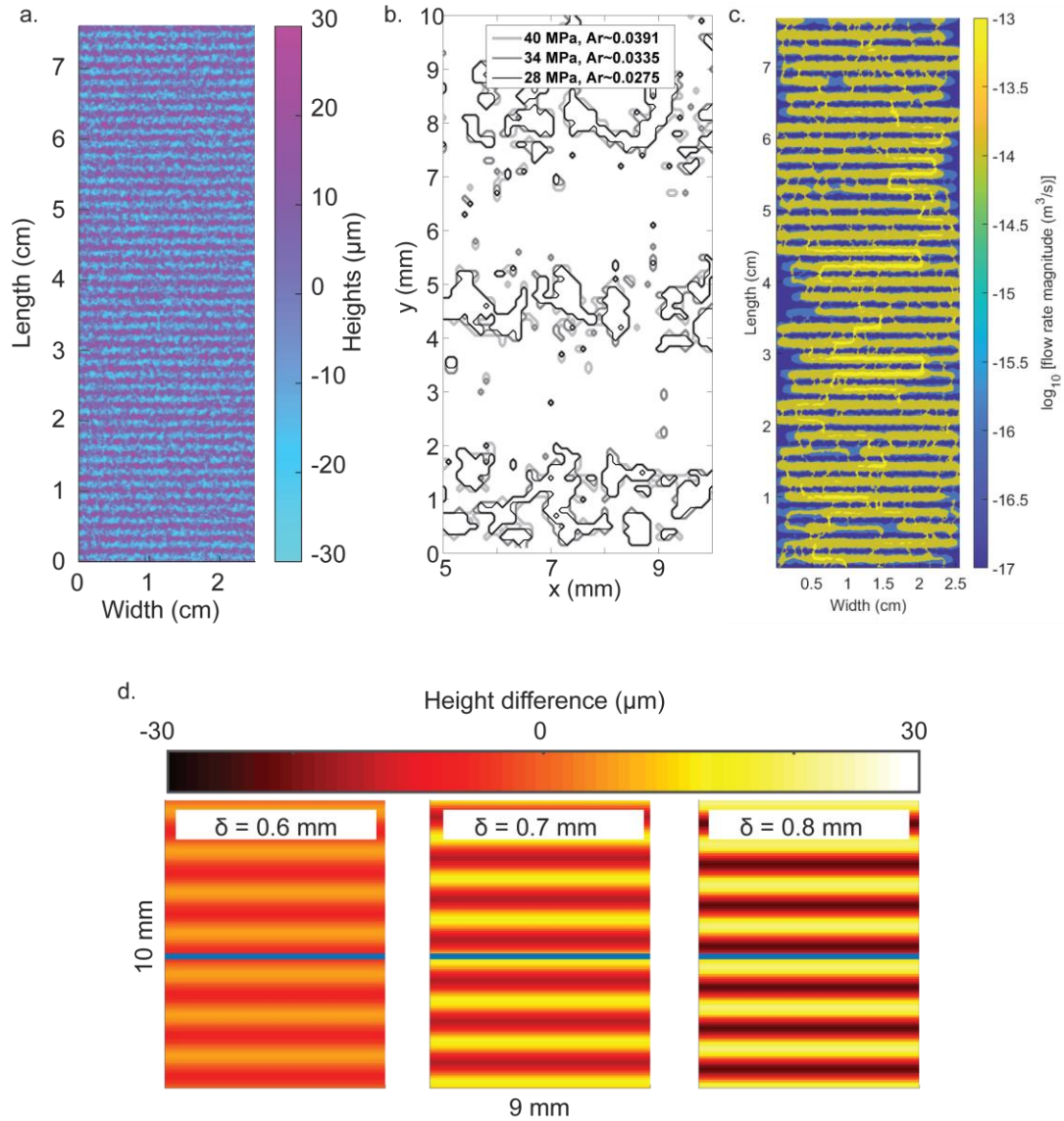
335 In order to simulate the effect of shear displacement on fracture transmissivity we simplified the
 336 problem to the shift between the two opposing artificial surfaces of a given displacement (Figure
 337 4d). For this model, two artificial rectangular surfaces (32 mm*64 mm; equivalent to the ellipsis
 338 area to simplify the problem) were generated with shifts of 0.1 mm in the y-direction and put into
 339 contact using the procedure described above. For each sample, a total of 10 surface pairs was
 340 computed to evaluate the evolution of transmissivity with increasing displacement up to 1 mm
 341 total displacement (Section 6.2).

342 3.4. Fluid flow calculation.

343 Finally, once that the contact area and geometrical aperture maps were extracted under different
 344 normal loads, the flow through the rough fractures was resolved. A finite volume formulation
 345 (Crandall et al., 2017; Brush and Thompson, 2003) was used to solve the Reynolds lubrication
 346 equation (Reynolds 1886). To apply the Reynolds lubrication equation (here simplified to the
 347 local cubic law (Zimmerman and Bodvarsson, 1996)) in the fracture, the main assumption is that
 348 the variations in aperture occur gradually in space over the fracture plane. This hypothesis seems
 349 reasonable because i) $\frac{h_{RMS}}{\lambda} \ll 1$, thus the vertical variations of roughness with respect to
 350 macroscopic wavelength are small, and ii) $\frac{L}{\lambda} > 10$, thus the aperture due to macroscopic
 351 wavelength is small compared to the fracture length. The Reynolds boundary layer
 352 approximation can therefore be expressed as (Brown, 1987; Zimmerman and Bodvarsson, 1996;
 353 Jaeger et al., 2007; Watanabe et al., 2008; 2009):

$$354 \int_S \rho \cdot \left[\frac{e_m^3}{12 \cdot \mu} \cdot \nabla p \right] \cdot \hat{n} \cdot dS = 0$$

355 where ρ and μ are the fluid density and viscosity respectively, $e_m(x,y)$ is the local mechanical (or
356 geometrical) aperture in the vertical direction (Brush and Thompson, 2003), S is the domain's
357 surface and \hat{n} is the outward unit normal vector to the local element. Details on the discretization
358 and resolution of the mass conservation equation above can be found in Brush and Thompson,
359 (2003) and Crandall et al. (2017). The imposed boundary conditions on the top and bottom ends
360 of the sample (y-axis) are Dirichlet (constant flow) pressure conditions $p_f = \pm 0.15$ MPa at $y = 0$
361 and $p_f = \pm 0.15$ MPa at $y = L$. The sign of the fluid pressures is opposed in all cases and they
362 depend on the flow sense that needs to be applied (top to bottom or bottom to top). Neumann
363 boundary conditions (no-flow) are applied at the lateral fracture boundaries $x = 0$ and $x = W$. (See
364 Figure 4 for details on the fracture geometry). The results from the finite volume code were
365 validated by comparison with a homemade finite difference code for flow calculation and with a
366 finite element code used with the commercial software Comsol multiphysics® (Annex 2).



367

368 Figure 4. Artificial surfaces: roughness, contact and fluid flow examples. a. Example of one
 369 artificially generated surface, colorbar accounts for the height distribution. b. results from contact
 370 simulations. Zoom on a 10 mm*5 mm part of the surface representing the contact area between
 371 two rough surfaces. Different confining pressures are shown (28, 34, 40 MPa are respectively the
 372 black, dark grey and light grey contours) c. Example of a flow through experiment performed
 373 with the contact area at $\sigma'_N = 28$ MPa as input. Colorbar shows the flow rate magnitude through
 374 the fracture in logarithmic scale. d. Difference of heights between the initial surface and surfaces

375 shifted of 0.6; 0.7 and 0.8 mm (left to right panels). Blue bar in the center of the zoomed surface
376 shows a position reference in the middle of the fracture.

377 While few studies have managed to simulate normal stresses in rough faults followed by the
378 fluid flow through them (Kang et al., 2016), to our knowledge, this is the first study to use a
379 combination of open-source numerical models for i) generating wavy, rough surfaces, ii)
380 simulating the contact under effect of normal stress and iii) the study of fluid flow through the
381 fractures.

382 **4. Experimental results**

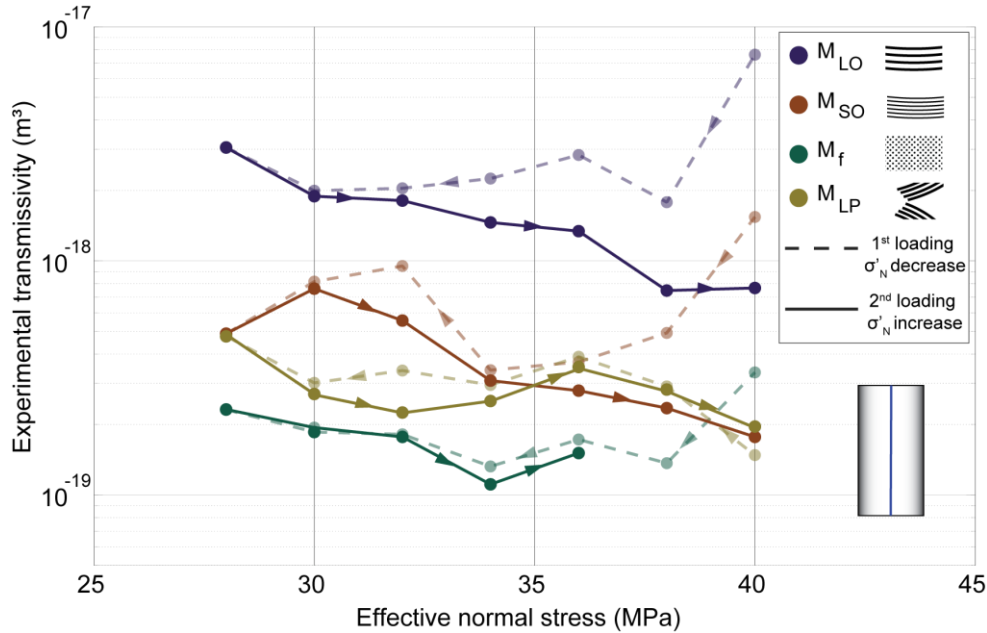
383 In all figures, a schematic legend is presented to show the customized sample's roughness. We
384 note that the samples prepared for flow-through experiments under normal loading are not the
385 same as those for experiments under shear loading, thus, slight differences between the sample's
386 roughness can be found for a same nomenclature.

387 4.1 Fluid flow through single fractures: normal loading.

388 Figure 5 shows the results of flow-through experiments obtained in terms of transmissivity as
389 function of effective confinement pressure. The dashed lines represent a first cycle where σ_3'
390 was decreased from 40 MPa to 28 MPa (by increasing fluid pressure). The full lines represent a
391 second cycle where the effective confinement was increased from 28 to 40 MPa. Note that the
392 measured transmissivities were always higher when σ_3' was decreased (first loading) than those
393 of the increasing cycle (second loading). To avoid issues related to this hysteretic behavior of the
394 fractures, the transmissivities that will be used hereafter are those of the increasing effective
395 confinement cycle (second loading) because they are representative of the fracture's
396 transmissivity under elastic behavior (Iwai., 1976; Witherspoon et al., 1980; Rutter and
397 Mecklenburgh, 2017; 2018).

398 The experimental sample M_{LO} (e.g large wavelength sub-orthogonal to fluid flow), showed
399 transmissivities ranging from $3.05e-18 \text{ m}^3$ at $\sigma_3'=28 \text{ MPa}$ down to $0.76 e-18 \text{ m}^3$ at $\sigma_3'=40 \text{ MPa}$.
400 Then, M_{SO} (e.g small wavelength sub-orthogonal to fluid flow), showed transmissivities half an
401 order of magnitude smaller than those of M_{LO} (ranging from $0.49e-18 \text{ m}^3$ down to $0.17 e-18 \text{ m}^3$
402 at $\sigma_3'=40 \text{ MPa}$). The sample with no imposed macroscopic wavelength, M_f had transmissivities
403 ranging from $0.23e-18 \text{ m}^3$ down to $0.15 e-18 \text{ m}^3$. The transmissivities were close to those of M_{LO}

404 and M_{SO} but the decay with increasing confinement smaller in this experiment with respect to the
 405 samples with macroscopic wavelength. The sample M_{LP} (e.g large wavelength sub-parallel to
 406 fluid flow), had transmissivities ranging from $0.48e-18 \text{ m}^3$ at $\sigma_3'=28 \text{ MPa}$ down to $0.20 e-18 \text{ m}^3$
 407 at $\sigma_3'=40 \text{ MPa}$. The transmissivities were almost half an order of magnitude lower than those of
 408 M_{LP} and close to those of M_{SP} .



409

410 Figure 5. Experimental results of normal loading experiments. Experimental fracture
 411 transmissivity function of the applied effective normal stress. Dashed lines represent effective
 412 pressure decrease and full lines represent effective pressure increase cycles.

413 4.2 Fluid flow through single fractures: shear loading.

414 Stress-displacement evolution.

415 Figure 6 (left axis) shows the shear stress versus axial displacement curves of all the conducted
 416 experiments. In all cases, shear stress first increased elastically (i.e. in a reversible manner) in
 417 response to increases in axial piston displacement (notice that due to the fault orientation and
 418 loading configuration, the normal stress also increased on the fault during elastic loading).
 419 During this stage, the faults were fully locked (Byerlee and Summers, 1975; Ohnaka, 2013;
 420 Scholz et al., 1972; Acosta et al., 2019). Then, once the shear strength of the faults was reached,
 421 reactivation occurred and shear stress versus displacement curves showed a roll-over (at
 422 displacements $d_{ro} \sim 0.11 - 0.20 \text{ mm}$) until reaching a steady-state where shear stress stayed

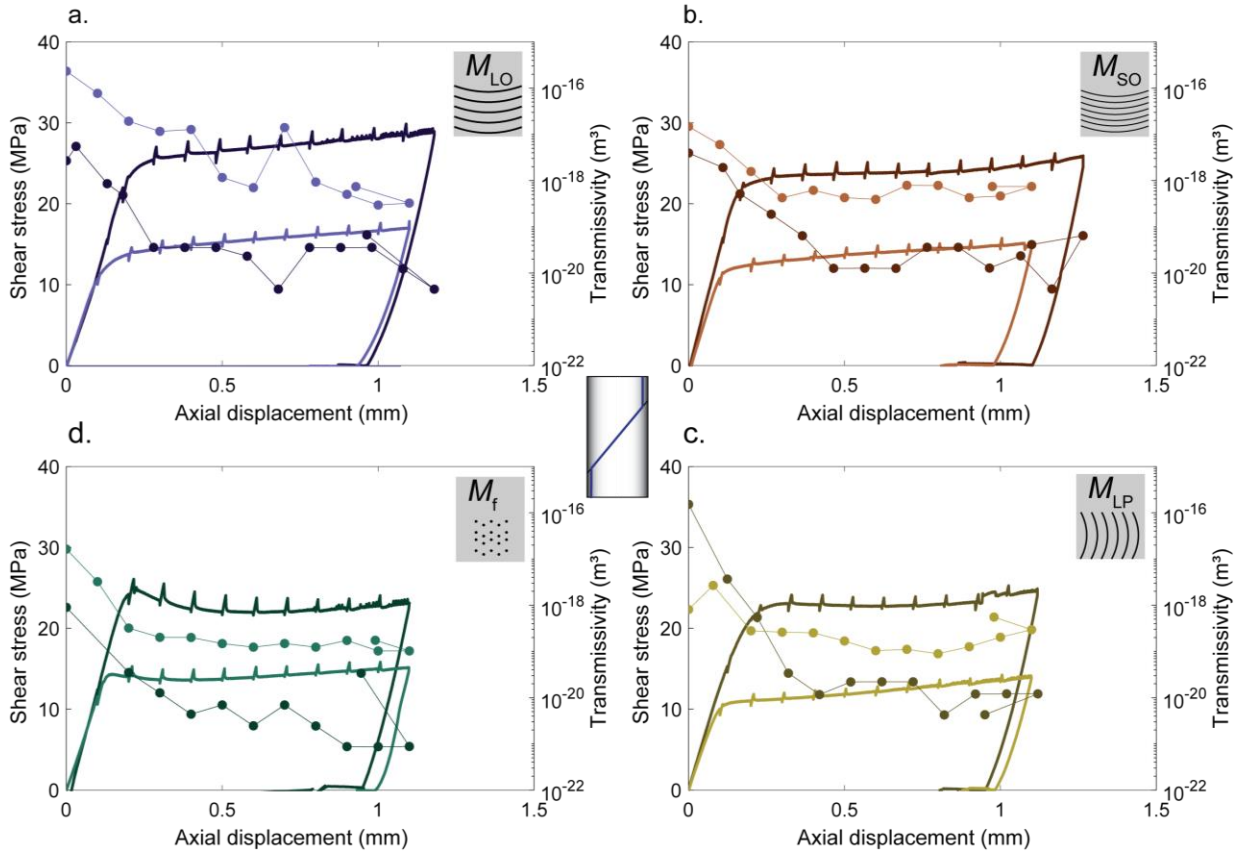
423 close-to-constant with increasing axial displacement. During this stage, the faults were unlocked
 424 and slipped at a near-to-constant rate. It is noticeable that, because axial displacement was
 425 increased step-wise to measure transmissivity, the fault showed an increase of shear strength at
 426 the start of every new displacement step. This “healing” behavior usually represented less than
 427 10% stress change with respect to fault’s shear strength. The peak values of stress and its
 428 relaxation are due to the time dependence of the fault’s real contact area (Dieterich, 1979;
 429 Dieterich and Kilgore, 1994). It is also noteworthy that all samples with an imposed macroscopic
 430 wavelength showed a near constant increase in shear stress with displacement after reactivation
 431 occurred (Figure 6a,b,d) at friction coefficients (τ/σ'_N) close to 0.5 (Table 1). The sample
 432 without macroscopic wavelength first showed a (very slow) stress drop at reactivation and then a
 433 near-constant increase in shear stress (Figure 6c).

434 The steady state shear strengths (τ_{ss}) in experiments conducted at $\sigma'_3 = 10$ MPa were $\tau_{ss} \sim 14 \pm$
 435 2 MPa with a maximum of 15.7 MPa for the sample M_{LO} and a minimum of 12.3 MPa for the
 436 sample M_{LP} . At $\sigma'_3 = 20$ MPa, τ_{ss} were in the range of 24 ± 3 MPa with a maximum of 27.0
 437 MPa for M_{LO} and a minimum of 22.0 MPa for M_{LP} . The steady state effective normal stress in
 438 experiments conducted at $\sigma'_3=10$ MPa ranged from 34.0 to 37.5 MPa. At $\sigma'_3=20$ MPa the
 439 effective normal stresses on the fault ranged from 58.7 to 66.3 MPa. As a result, all the
 440 experiments presented state friction values in the range $f_{ss} \sim 0.54$ to 0.61 ± 0.02 , in agreement
 441 with Byerlee’s Rule (Byerlee, 1978). A compilation of the values is given in Table 1.

442 Transmissivity results.

443 The transmissivities measured during shear loading experiments are shown in Figure 6 (right
 444 axes). In experiments conducted at $\sigma'_3=10$ MPa, the initial transmissivities (kt_0 ; e.g. with no
 445 applied deviatoric stress and at zero axial displacement) ranged from $\sim 2.33 \cdot 10^{-16}$ to $2.42 \cdot 10^{-18}$
 446 m^2 with maxima and minima for samples M_{LO} and M_{LP} respectively. With increasing axial
 447 displacement, transmissivity sharply decreased during reversible fault loading (usually of more
 448 than one order of magnitude). For the experiments M_{LO} and M_{LP} , it dropped to values of
 449 $1.27 \cdot 10^{-17}$ and $2.60 \cdot 10^{-19}$ m^2 respectively (e.g. of ~ 1 order of magnitude) at the onset of
 450 reactivation respectively. During fault reactivation, transmissivity usually slightly decreased
 451 overall; with local rises (to kt_{ss}^{max}) and drops (to kt_{ss}^{min}) of lesser magnitude than the decrease
 452 during elastic loading. Finally, after unloading, transmissivity (kt_{unl}) slightly increased in most
 453 cases (Except for sample M_{LP} deformed at $\sigma'_3 = 20$ MPa) but was far from being recovered to

454 kt_0 . Transmissivity after unloading was usually close to the value found at the onset of
 455 reactivation. For experiments conducted at $\sigma'_3=20$ MPa, kt_0 were 3 to 42 times larger than at
 456 $\sigma'_3=10$ MPa (except for M_{LP} where kt_0 was surprisingly two orders of magnitude higher at $\sigma'_3 =$
 457 20 MPa). At the onset of reactivation, $kt_{ss}(\sigma'_3 = 20$ MPa) were 13 to 392 times lower than kt_{ss}
 458 at $\sigma'_3=10$ MPa). Finally, at unloading kt_{unl} was 11 to 105 times lower at larger confining stress.



459

460 Figure 6. Coupled evolution of fault's shear stress and transmissivity in response to shear
 461 loading. In all panels, left y-axis shows shear stress (note that normal stress also increased during
 462 shear loading), right y-axis shows fault's transmissivity (circles) and x-axis is the axial
 463 displacement. Darker and lighter colors represent experiments conducted at 20 and 10 MPa
 464 effective confinement pressure respectively. a. Experiments on sample M_{LO} (long wavelength,
 465 grooves sub-orthogonal to fluid flow and shear displacement). b. Experiments on sample M_{SO}
 466 (small wavelength, grooves sub-orthogonal to fluid flow and shear displacement). c. Experiments

467 on sample M_f (with no macroscopic imposed wavelength). d. Experiments on sample M_{LP} (long
468 wavelength, grooves sub-parallel to fluid flow and shear displacement).

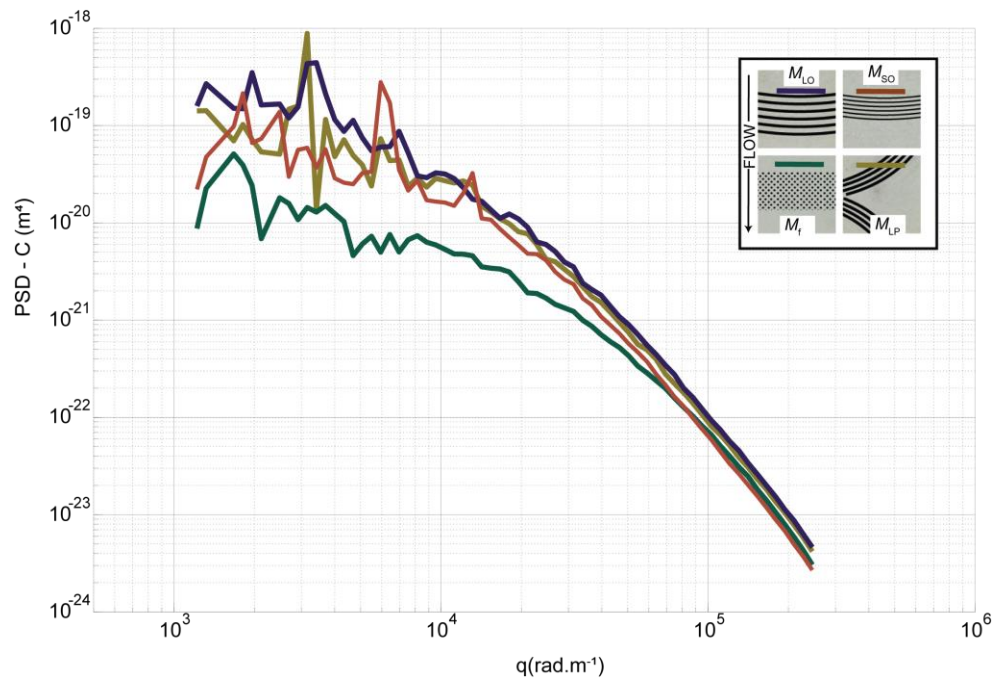
469 **5. Microstructures**

470 5.1 Initial sample roughness.

471 Figure 7 shows the PSD curves for all initial experimental surfaces. The 2D PSD curves
472 presented 2 sections: A first, ‘flat’ part where the power spectral density was close to constant
473 with increasing wavenumber until the roll off wavenumber q_r . And a second part, presenting a
474 power law dependence on wavenumber. The slope in a log-log plot is $-2 \cdot (H + 1)$ with H the
475 Hurst exponent (Candela et al., 2012; Jacobs et al., 2017). The Hurst exponent characterizes the
476 power law decay of PSD with increasing wavelength. In that sense, H usually characterizes the
477 fractal dimension of a surface (Candela, 2012; Jacobs et al., 2017 and references therein).

478 Finally, the area under the PSD curves represents the Root Mean Square height (h_{RMS}) which is
479 the standard deviation of the heights distribution (Candela., 2012; Jacobs et al., 2017 and
480 references therein).

481 Prior deformation, for $q < q_r$, the samples M_{LO} had amplitudes ($C(q < q_r) \sim 2 \cdot 10^{-19} \text{ m}^4$), and the
482 samples M_{SO} and M_{LP} had smaller amplitude prior to roll off ($C(q < q_r) \sim 7-8 \cdot 10^{-20} \text{ m}^4$). Finally,
483 the sample with no macroscopic wavelength - M_f - had the smallest amplitudes prior to roll-off
484 ($C(q < q_r) \sim 1 \cdot 10^{-20} \text{ m}^4$). The roll of wavenumbers were the smallest for M_{LO} , M_{LP} and M_{SO}
485 ($q_r \sim 6900 \text{ rad} \cdot \text{m}^{-1}$). q_r were larger for the sample with no macroscopic wavelength M_f ($q_r \sim 10000$
486 $\text{rad} \cdot \text{m}^{-1}$) (Table 1). Regarding Hurst exponents determined from the slope of the PSD curves, the
487 samples M_{LO} and M_{SO} had H respectively 0.47 and 0.60. The sample with no macroscopic
488 wavelength M_f had lower $H \sim 0.44$ and finally M_{LP} had $H \sim 0.59$. The largest h_{RMS} were calculated
489 for M_{LO} and M_{SO} (~ 9.0 and $8.0 \mu\text{m}$ respectively). Then, M_f had lower $h_{RMS} \sim 4.5 \mu\text{m}$ and finally
490 M_{LP} had $h_{RMS} \sim 7.5 \mu\text{m}$. The sample M_{LO} had a macroscopic wavelength $\lambda = 1.7 \text{ mm}$ with while
491 the M_{SO} surfaces had $\lambda = 0.9 \text{ mm}$. Both samples had an imposed wavelength amplitude of $11 \mu\text{m}$.
492 Finally, M_{LP} had $\lambda = 1.7 \text{ mm}$ with an amplitude of $\sim 9 \mu\text{m}$. The results are summarized in Table 2.

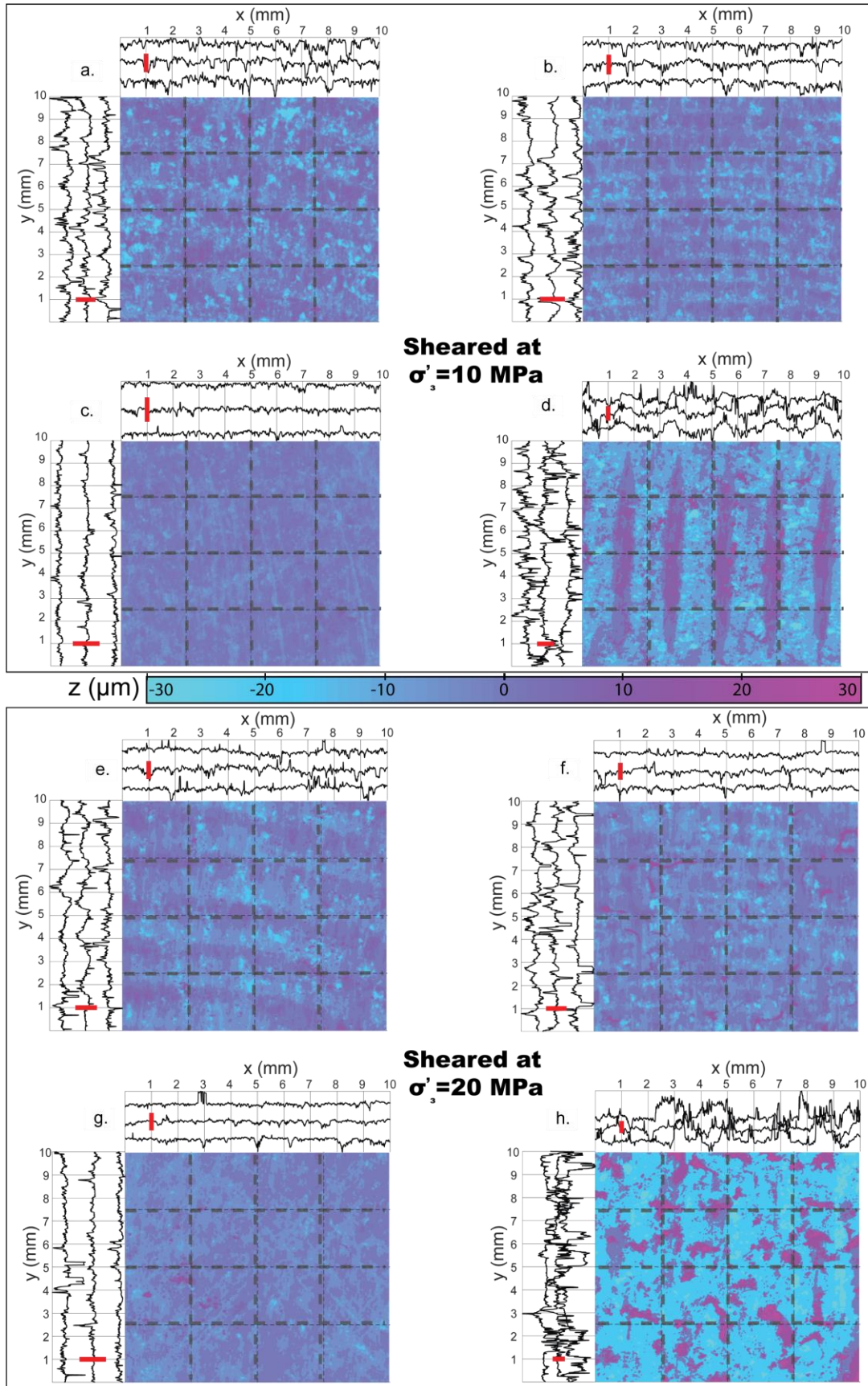


493

494 Figure 7. Results of surface roughness measurements for all the experimental samples. 2D-Power
 495 spectral density of height distribution. Insets show which sample corresponds to which PSD
 496 curve.

497 5.2 Post-deformation sample roughness.

498 Fault surface roughness changed when shear displacement increased. The topography maps after
 499 deformation are shown in Figure 8 (at low confining pressure in panels a-d and at high confining
 500 pressure in panels e-h). Note that a different sample was used for each confining pressure
 501 experiment so as to initiate loading in similar conditions. Overall, the post-mortem samples
 502 showed evidence of striation (grooves in the sense of shear), as well as changes in the height
 503 distributions (Figure 8). Evidence was found of gouge formation during shearing with pervasive
 504 presence of microscopic particles in low height zones. Larger amounts of gouge were generated
 505 in experiments at higher confining pressure. It is noticeable that at both effective confinements,
 506 the samples M_{LP} (e.g. with grooves sub-parallel to the shear sense), showed very large changes
 507 in the surface characteristics (Figure 8d,h). There, the initial wavelengths were unrecognizable
 508 from topography measurements while in all the other experiments, the initial surface topography
 509 could be partly recognized.

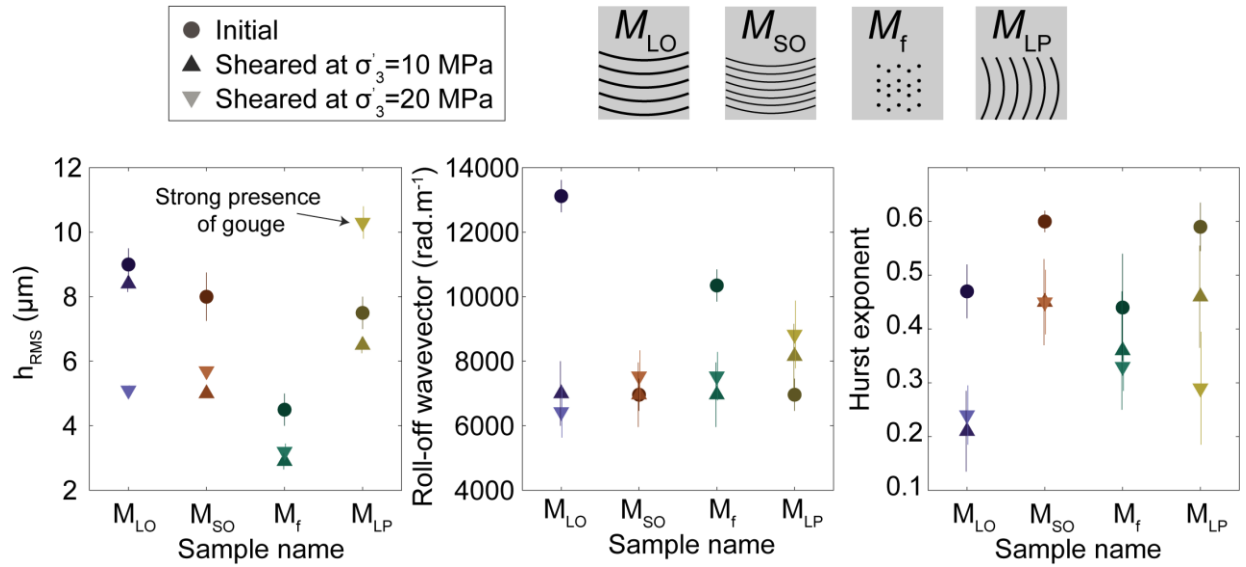


511 Figure 8. Post-mortem surface topography maps. Colorbar represents the measured heights over
 512 the area. The transects in x-axis and y-axis in dotted lines are presented in the top and left plots
 513 respectively. For reference, a red bar represents 30 micrometer height. a-d Maps of post-
 514 deformation experiments at 10 MPa effective confinement for samples M_{LO} (panel a.); M_{SO}
 515 (panel b.); M_f (panel c.); M_{LP} (panel d.); e-h Maps of post-deformation experiments at 20 MPa
 516 effective confinement for samples M_{LO} (panel e.); M_{SO} (panel f.); M_f (panel g.); M_{LP} (panel h.).
 517 Surface topographies can be compared with Figure 1a-d.

518

519 To study the statistical properties of these surfaces, the PSD's were computed again on post-
 520 mortem topography maps and analyzed in the same manner as those of intact surfaces. The PSD
 521 curves showed a change in shape. Indeed, the previously 'flat' part of the PSD's showed an
 522 overall slope after deformation, adding additional complexity to the estimation of the roll-off
 523 wavevector for post-mortem samples. The results are compiled in Table 3 and summarized in
 524 Figure 9. The root mean square of heights h_{RMS} decreased after shearing in all cases (except for
 525 the sample M_{LP} deformed at σ'_3 30 MPa) (Figure 9a). No tendency was observed regarding h_{RMS}
 526 with respect to the confining pressure at which the samples were deformed. q_r was here
 527 estimated where the slope of the PSD curves changed. With that estimation of q_r , an overall
 528 decrease was observed for all samples after shearing with the measurements converging on all
 529 samples towards values of $\sim 5000 - 8000 \text{ rad.m}^{-1}$ (Figure 10b). Finally, the Hurst exponent also
 530 showed an overall decrease after shearing for all samples with slightly lower values of H in
 531 experiments at higher effective confinement (Figure 9c).

532



533

534 Figure 9. Pre-and-post-mortem roughness parameters. Circles represent initial surfaces with the
 535 estimated error. Upward triangles represent post-mortem samples deformed at 10 MPa effective
 536 confinement and downward triangles represent experiments at 20 MPa effective confinement. a.
 537 root mean square of heights parameter. b. roll-off wavevector. c. Hurst exponent.

538

Sample name	Grooves ^a , ⊥, no	Deformed	σ'_3 MPa	λ^b mm	$err \lambda^c$ mm	Amp ^d μm	err Amp ^c μm	h_{rms}^e μm	$err h_{rms}^f$ μm	q_r^g rad.m^{-1}	$err q_r^h$ rad.m^{-1}	H^i -	$err H^j$ -
M_{LO}	⊥	intact	0	1.7	0.1	11	2	9	1	6963	1000	0.47	0.1
M_{SO}	⊥	intact	0	0.9	0.1	11	2	8	1.5	6963	1000	0.6	0.04
M_f	no	intact	0	0	0	0	0	4.5	1	10350	1000	0.44	0.2
M_{LP}		intact	0	1.7	0.1	11	2	7.5	1	6963	1000	0.59	0.09
M_{LO}	⊥	sheared	10	1.7	0.1	15	5	8.4	0.5	7000	2000	0.21	0.15
M_{SO}	⊥	sheared	10	0.9	0.1	15	5	5	0.2	6963	2000	0.45	0.16
M_f	no	sheared	10	0	0	0	0	2.9	0.5	6963	2000	0.36	0.22
M_{LP}		sheared	10	0	0.1	17	5	6.5	0.5	8158	2000	0.46	0.19
M_{LO}	⊥	sheared	20	1.7	0.1	15	5	5.1	0.3	6433	1600	0.24	0.11
M_{SO}	⊥	sheared	20	0.9	0.1	15	5	5.7	0.2	7537	1600	0.45	0.12
M_f	no	sheared	20	0	0	0	0	3.2	0.5	7537	1500	0.33	0.09
M_{LP}		sheared	20	2	0	35	10	10.3	1	8831	2100	0.29	0.21

^a parallel or orthogonal to fluid flow^b determined by counting the number of wavelengths in a given area^c determined from the difference between the six prepared half-samples^d determined from the roughness profiles^e determined from the integral of radially averaged 2D-PSD and from the standard deviation of heights^f determined from the differences between integral of radially averaged PSD and from the standard deviation of heights and the 6 half samples^g determined from the flat part of radially averaged PSD^h determined from the difference between the 6 prepared half samplesⁱ determined from the self-similar part of radially averaged PSD^j determined from the difference between the 6 prepared half samples and from the maximum and minimum slope taken on a moving window of half an order of magnitude

539

540

Table 2. Experimental samples roughness.

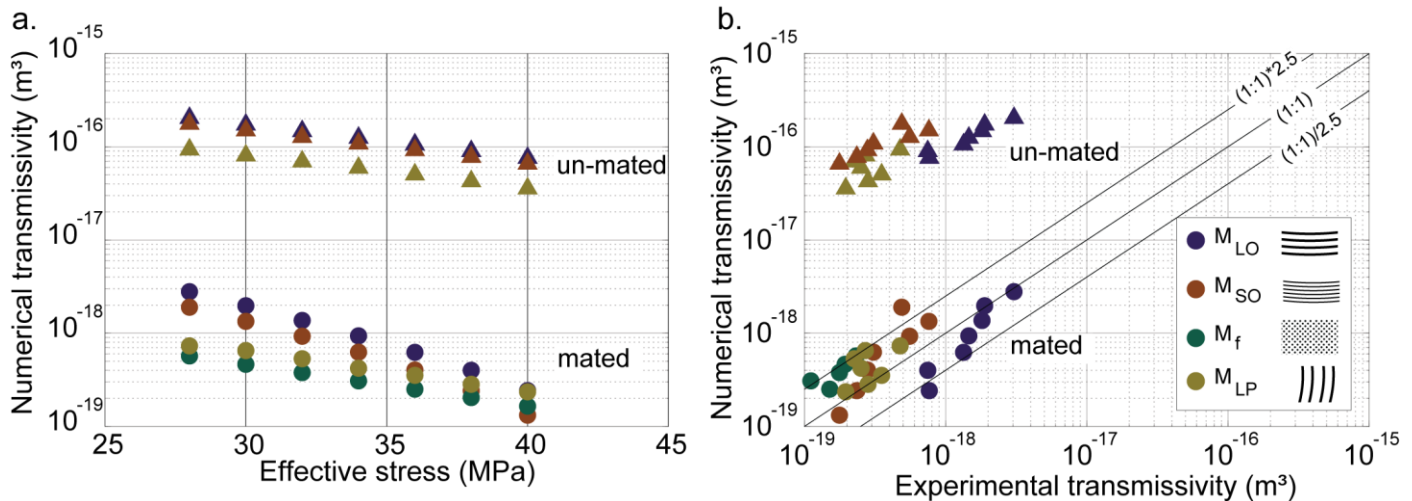
541 **6 Discussion.**

542 6.1 Influence of roughness parameters on fracture transmissivity under normal loading.

543 The hydraulic transport properties of rough fractures submitted to normal stress are
544 highly dependent on the surface geometry and roughness parameters (Section 4.2; Chen et al.,
545 2000; Watanabe et al., 2008; 2009; Patir and Cheng, 1978; Iwai, 1976; Pyrak-Nolte et al., 1988;
546 Walsh, 1981; Watanabe et al., 2008; 2009; Iwai, 1976; Witherspoon et al., 1980; Rutter and
547 Mecklenburgh, 2017; 2018). We now study the flow through wavy rough fractures submitted to
548 normal loading only in this subsection. As described in section 3, first artificial surfaces with
549 roughness parameters similar to those measured experimentally were generated. Then, the
550 contact between the surfaces at given loads was simulated, and finally the flow through the
551 fractures was computed. The numerical results are presented in Figure 10a corresponding to the
552 samples tested experimentally. For all samples, two types of numerical simulations were
553 conducted. One where the large wavelengths were in peak-to-peak contact (e.g non-mated or
554 non-imbricated surfaces, Figure 10 triangles). In those cases, the resolved numerical
555 transmissivities were more than two orders of magnitude larger than those measured
556 experimentally (Figure 5). Another set of numerical simulations was conducted where the large
557 wavelengths were in peak-to-valley contact (e.g fully mated surfaces, Figure 10a circles). In this
558 case, the resolved numerical transmissivities ranged from $0.50\text{e-}18 \text{ m}^2$ at $\sigma_3' = 28 \text{ MPa}$ down to
559 $0.20\text{e-}18 \text{ m}^2$ at $\sigma_3' = 40 \text{ MPa}$, for sample M_{LP} as an example. The fully mated transmissivity
560 results are in strong in compatibility with experimental results. This highlights the strong
561 influence of flow channeling on fracture hydraulic transport capacity which cannot be neglected
562 in the analysis (Watanabe et al., 2009; Shvarts and Yastrebov., 2018; Shvarts, 2019).
563 We observe that for all samples, the numerical transmissivity has an exponential decay with
564 increasing normal stress (the plot is log-normal) as $kt(\sigma_N') = a \cdot e^{-b\sigma_N'}$, with a and b two
565 fitting parameters. The sample's initial geometry seems to condition the parameters a and b .
566 With larger values of the b parameter in samples M_{LO} ($b_{M_{LO}} = 0.190$) and M_{SO} ($b_{M_{SO}} = 0.198$).
567 Then, an intermediate value of b is found for sample M_f ($b_{M_f} = 0.103$) and the smaller one for
568 M_{LP} ($b_{M_{LP}} = 0.099$). To summarize, samples with grooves perpendicular to fluid flow are more
569 sensitive to normal stress than samples with no roughness which are in turn more sensitive than
570 samples with grooves sub-parallel to fluid flow. The transmissivity decay with increasing normal

571 stress has been seen with i) near exponential decays (Iwai, 1976; Witherspoon et al., 1980;
 572 Pyrak-Nolte et al., 1988), ii) logarithmic decay (Walsh, 1981), or iii) through more complex
 573 decays depending on heterogeneous topographies (Watanabe et al., 2008; 2009) and loading
 574 paths (Iwai, 1976; Witherspoon et al., 1980; Rutter and Mecklenburgh, 2017; 2018).

575 From the numerical procedure developed in this work, one can expect a near exponential
 576 decay of transmissivity at the working experimental normal stresses for the modeled carbonate
 577 rock. In turn, the experimental results show a small scatter towards the exponential decay
 578 predicted by the model. Which can be due to i) the loading path (e.g. hysteresis; Iwai, 1976;
 579 Witherspoon et al., 1980; Rutter and Mecklenburgh, 2017; 2018); ii) imperfections in the
 580 experimental contacts with respect to the numerical model; or iii) small non-linearities in fluid
 581 flow in real sample surfaces (Zimmerman and Bodvarsson., 1996) which are not considered in
 582 the Reynolds lubrication approximation for the simulations. Overall, the numerical results are
 583 remarkably consistent with the experimental data, as shown by the small deviation of data from
 584 the 1:1 slope in Figure 10b. In the numerical simulations, more than 90% of the points are
 585 contained within a factor 2.5 from the experimental data.



586
 587 Figure 10. Flow through numerical results. a. Numerical fracture transmissivity function of
 588 effective stress applied on the fracture. b. Numerical transmissivity function of experimental
 589 transmissivity. In both panels, triangles represent the numerical results from samples with an un-
 590 mated configuration. In panel b. the black lines represent a slope of 1 and a deviation with a
 591 factor 2.5 to that line. Note that more than 90 % of the data points were contained within that
 592 factor. The numerical model developed gives good agreement with the experimental hydraulic
 593 transport properties measured under normal loading.

594

595 The goal of the following section is to isolate the roughness parameters that have stronger
 596 control on hydraulic transport properties through a parametric analysis of the numerical
 597 procedure. First, the parameters are isolated in absence of macroscopic grooves and then, the
 598 effect of the large-scale wavelength with grooves perpendicular to the fluid flow is studied.

599

600 Flat rough surfaces (absence of macroscopic grooves)

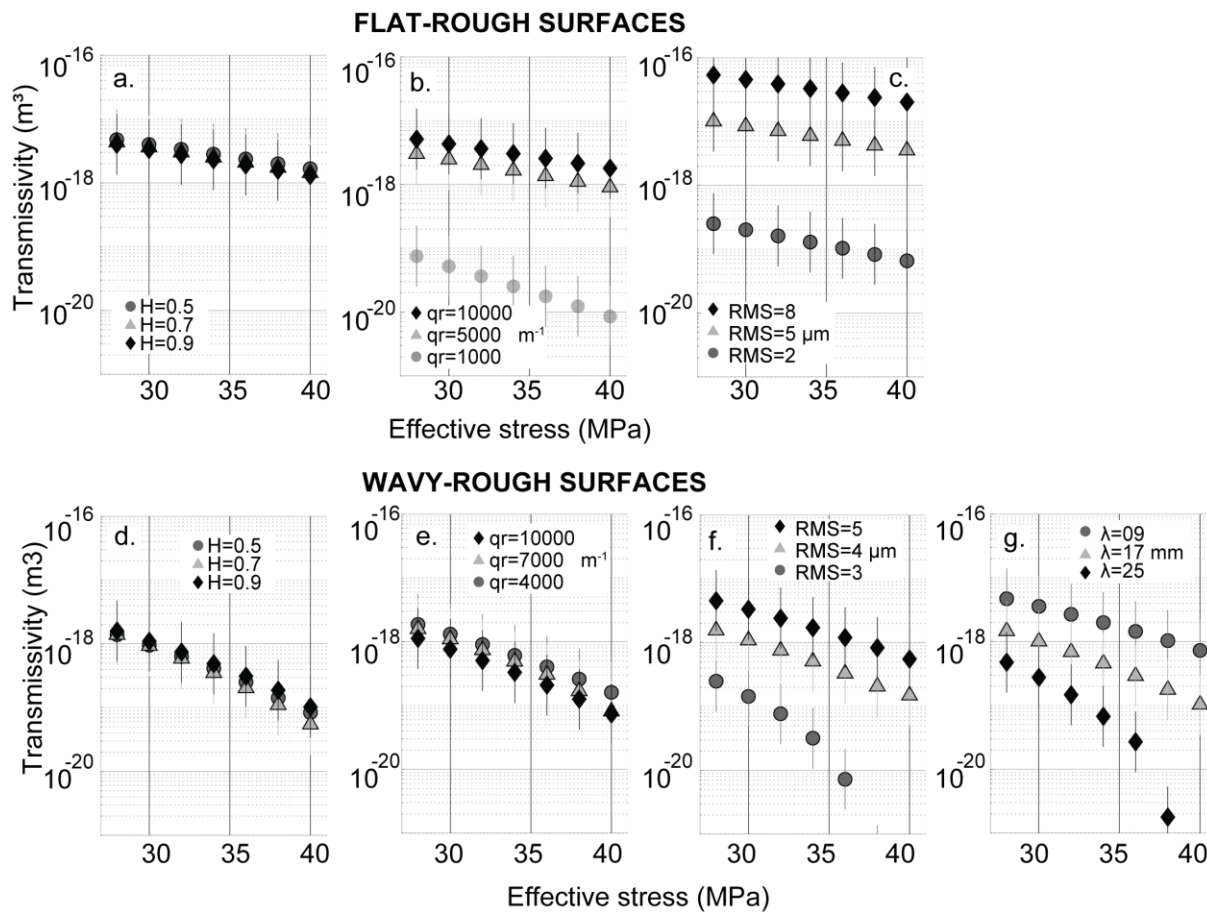
601

602 First, the roughness properties are analyzed for rough surfaces without imposed
 603 wavelength to avoid bias from the macroscopic grooves on all other parameters (H ; q_r ; h_{RMS}).
 604 Artificial surfaces with $L = 75$ mm (length) and $W = 25$ mm (width) with 768×256 nodes were
 605 created and tested through the same numerical procedure described in section 3. The steady
 606 parameters (the parameters that do not change when only one of the other parameters is varied)
 607 are $H = 0.6$, $q_r = 8000$ rad.m⁻¹ and $h_{RMS} = 8$ μm. Hurst exponents are varied from 0.5 to 0.9
 608 (values that can be found in natural and experimental faults; Brown and Scholz, 1985; Candela et
 609 al., 2009), roll-of wave-vectors are varied from 1000 to 10000 rad.m⁻¹ and h_{RMS} are varied from
 610 2 to 8 μm. Results are shown in Figure 11.

611

- 612 - The Hurst exponent characterizes the power law decay of PSD with increasing
 613 wavelength. Thus, it characterizes the self-affinity of a surface (Candela, 2009;
 614 Renard et al., 2013; Jacobs et al., 2017 and references therein). Changes from 0.5 to
 615 0.9 in Hurst exponent alone (Figure 11a), do not show large changes in transmissivity
 616 (30 to 60 % lower for the lowest tested Hurst exponent) of the simulated fractures.
- 617 - q_r is the wave-vector where the PSD curves change from a close-to-constant value to
 618 a power law distribution with increasing wavenumber (with a power $-2(H + 1)$).
 619 Physically this number represents the wavevector where the surface heights depart
 620 from a self-affine distribution. From Figure 11b, q_r has a strong influence on
 621 transmissivity only for $q_r < 5000$ rad.m⁻¹. Under our experimental conditions q_r is
 622 often comprised between 5000 and 10000 rad.m⁻¹ (Table 3). In that range, q_r
 623 variation has little influence over the transmissivity response.

624 - The root mean square of the height distribution (h_{RMS}) corresponds to its standard
 625 deviation, thus to the dispersion of heights around the mean value. The higher h_{RMS} ,
 626 the ‘rougher’ the surface (Brown and Scholz, 1985, Candela et al., 2009; 2012;
 627 Renard et al., 2013; Jacobs, 2017) and the higher the hydraulic apertures. From
 628 Figure 11c, we observe that h_{RMS} has the largest influence over the transmissivity
 629 response of the flat-rough fractures. Increase of 2 to 8 μm results in over three orders
 630 of magnitude difference transmissivity. The lower h_{RMS} height, the flatter the
 631 surfaces, hence, under normal load, the better they match to each other and the
 632 smaller their mechanical and hydraulic apertures.



633

634 Figure 11. Parametric analysis. a-c. For flat rough surfaces. All panels show fracture
 635 transmissivity function of the simulated effective stress. Error bars correspond to a factor 2.5 in
 636 transmissivity which is taken as model’s accuracy. a. Variation of the Hurst exponent alone. b.
 637 Variation of the roll-off wave vector alone. Note that a wavevector of 1000 $\text{rad}\cdot\text{m}^{-1}$ is widely out
 638 of the range from experimental samples. c. Variation of h_{RMS} . The base values for this

639 parametric analysis are given in the text. e-g. Parametric analysis for wavy-rough surfaces. a.
 640 Variation of the Hurst exponent alone. b. Variation of the roll-off wavevector alone. c. Variation
 641 of the whole h_{RMS} . d. Variation of the macroscopic wavelength. The base values for this
 642 parametric analysis are given in the text.

643
 644 Wavy rough surfaces (in presence of macroscopic grooves)

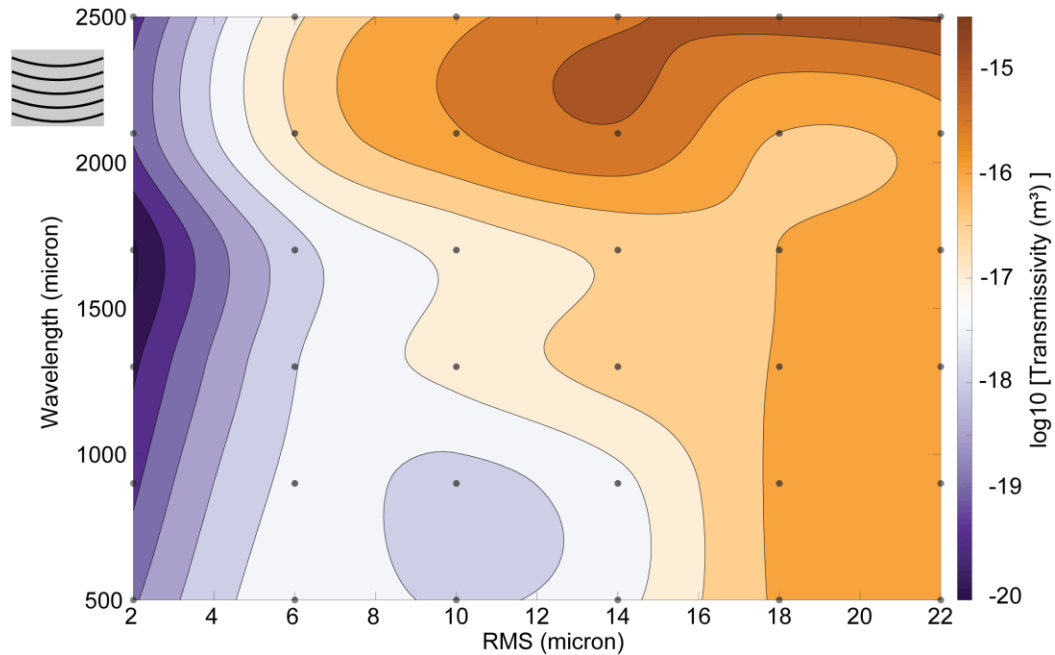
645 To study the effect of the macroscopic wavelength on fracture's transmissivity, artificial
 646 surfaces were generated by overlaying a surface with a macroscopic wavelength and a flat rough
 647 surface such that the overall h_{RMS} equals the targeted value. The steady parameters are $H = 0.6$,
 648 $q_r = 7000 \text{ rad.m}^{-1}$ and $h_{RMS} = 4 \mu\text{m}$ and wavelength $\lambda = 1.7 \text{ mm}$. These reference values are
 649 taken from experimental observations. Hurst exponents are varied from 0.5 to 0.9, roll-of wave
 650 vectors are varied from 4000 to 10000 rad.m^{-1} , h_{RMS} are varied from 3 to 5 μm and wavelengths
 651 λ from 0.9 to 2.5 μm . Results are shown in Figure 11d-g.

652 Figures 11d,e show again that H and q_r alone have little influence on the transmissivity of wavy
 653 rough surfaces (changes of 30 to 60% in transmissivity for a change of 0.4 in H and 3 to 5 times
 654 increase in transmissivity for a variation of 6000 in q_r). On the other hand, h_{RMS} has strong
 655 control on the fracture's transmissivity (Figure 11f). Indeed, at $\sigma_3' = 35 \text{ MPa}$, the transmissivity
 656 is more than 3 orders of magnitude larger from $h_{RMS} \sim 3 \mu\text{m}$ to 5 μm . We observe that for a
 657 change in λ from 0.9 to 2.5 cm, at $\sigma_3' = 35 \text{ MPa}$, the increase in transmissivity is more than 3
 658 orders of magnitude (Figure 11g) highlighting the strong control of the wavelength on the
 659 hydraulic transport capacity of the rock fracture.

660 We performed thirty-six additional simulations to explore the combined effects of
 661 wavelength and standard deviation of heights on fracture's transmissivity (these simulations
 662 were performed with $\sigma_N' = 28 \text{ MPa}$ as an example). The results are shown in Figure 12. The
 663 evolution of transmissivity is strongly non-monotonic in the parameter space. A combination of
 664 small λ and low h_{RMS} naturally results in low transmissivities. Nevertheless, low λ (500 -1000
 665 μm) and intermediate h_{RMS} (10 μm) can result in regions of lower transmissivities than its
 666 surroundings. At intermediate λ ($\sim 1500 \mu\text{m}$), an increment of h_{RMS} results in less increase in
 667 transmissivity than at higher λ ($\sim 2100 \mu\text{m}$) for example. We conclude from this analysis that, for
 668 complex topographies, the transmissivity of wavy rough fractures from averaged height values
 669 (h_{RMS} only for example) needs to be evaluated with care (Renshaw, 1995; Zimmerman and

670 Bodvarsson., 1996; Brown, 1987; Hakami, 1989; Piggott and Ellsworth., 1992; Patir and Cheng,
671 1978).

672



673

674 Figure 12. Contour plot of transmissivity of rough wavy surfaces (grooves sub-orthogonal to
675 fluid flow). The fault's transmissivity (in log scale) is computed as function of the root-mean-
676 square roughness (h_{RMS}) and the macroscopic wavelength for artificial wavy-rough surfaces.
677 Effective pressure considered for this plot is 28 MPa.

678 6.2 Influence of reversible shear loading and of irreversible shear displacement on
679 transmissivity.

680 The effect of reversible shear loading on transmissivity (prior the onset of sliding).

681

682 Elastic shear loading strongly decreased transmissivity under all tested conditions. The
683 change in transmissivity is due to the increase in both normal and shear stress on the fracture
684 prior to sliding (note that this type of loading is more common in natural faults than a shear
685 loading at constant normal stress). In order to isolate the effect of reversible shear load, we now
686 compare the results from the validated numerical model (for fractures submitted to normal stress
687 only) to the experimental results obtained under both shear and normal stress. To do this, the
688 model results of fracture transmissivity function of normal stress were fitted with an exponential

689 decay as $kt(\sigma'_N) = a \cdot e^{-b\sigma'_N}$ (full colored lines in Figure 13). The values of a and b are given in
 690 Figure 13. Then, we compare the model values to experimental results of fracture transmissivity
 691 submitted to both normal and shear stress during reversible (elastic) loading (filled circles in
 692 Figure 13; darker colors for higher effective confinement). Note that all deviations from the
 693 (normal loading) model results from the effect of shear loads shear loads in this configuration.
 694 We observe that reversible shear load has very little effect on transmissivity. It either increases or
 695 decreases fault transmissivity with respect to the case where only normal load was applied.
 696 When the sample had no macroscopic roughness (M_f , Figure 13c), the transmissivity mostly
 697 decreased, in particular when high (normal and shear) stress was applied. Similar observations
 698 were observed previously in smooth hard-rock surfaces at high stresses (Rutter and
 699 Mecklenburgh, 2017; 2018). In the case of sample M_{LO} (Figure 13a), transmissivity rose of
 700 almost two orders of magnitude under all stress conditions. For sample M_{SO} (Figure 13b),
 701 transmissivity was not affected by shear stress at low confinement (first two points from left to
 702 right) but increased at high confining pressure (3rd and 4th points from left to right). Finally, for
 703 sample M_{LP} (Figure 13d), the transmissivity usually decreased except for one point that seems to
 704 be an outlier in the transmissivity evolution (Figure 6d, displacement < 0.1 mm).

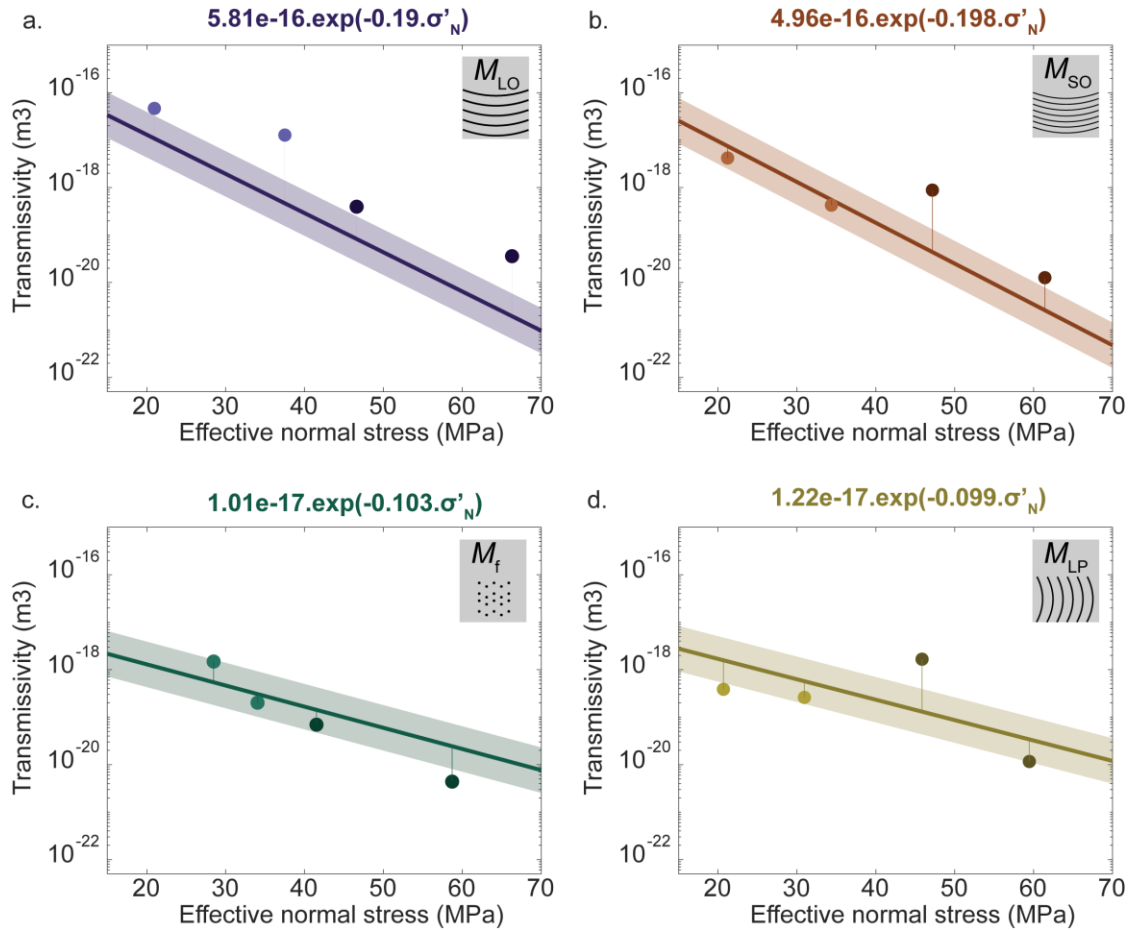
705 An increase in transmissivity due to the application of reversible shear load alone should
 706 be due to a decrease of the real contact area with increasing shear stress because the hydraulic
 707 aperture (h_H) is a function of the real contact area (A_r) as (Walsh, 1981):

$$708 \quad h_H = h_M \cdot \left(\frac{1 - A_r}{1 + A_r} \right)^{\frac{1}{3}}$$

709 where h_M is the geometrical aperture of the fracture surface. The evolution of the real contact
 710 area with increasing shear in a frictional contact is today a controversial issue in the contact
 711 mechanics community. On the one hand, several studies have shown a decrease of the real
 712 contact area with increasing shear stress prior to (and at the onset of) sliding in mortar rock
 713 replicas (Grasselli and Egger, 2003; Park and Song, 2013); on hard polymers (BenDavid et al.,
 714 2010; Svetlizky and Fineberg, 2014; Bayart et al., 2016); and on soft polymers (Sahli et al.,
 715 2018). On the other hand, experiments in hard, coated polymers (Bay and Wanheim, 1976) and
 716 in polystyrene-on-glass contacts (Weber et al., 2019) have shown that the real contact area in
 717 turn increases with shear stress and initial displacement due to a mechanical degradation of the
 718 asperities (plastic deformation). By isolating the effect of normal stress and shear stress

719 separately on transmissivity, our results show that the application of reversible shear load is not
720 the only factor affecting fracture transmissivity but rather the combination of geometry and
721 stress, even though its effect is small. Indeed, both samples with macroscopic grooves sub-
722 orthogonal to shear showed the largest increase of transmissivity. In experiments similar as those
723 conducted here but in smooth, hard- rock samples (Rutter and Mecklenburgh, 2017; 2018), the
724 increase of shear stress at constant normal stress led to a very slight decrease in fault
725 transmissivity at the onset of reactivation. There, the authors inferred that the slight
726 transmissivity decrease was due to asperity collapse during shear loading. In our experiments, it
727 seems therefore reasonable that during elastic loading only (e.g. while no permanent changes in
728 surface topography occur), the transmissivity varies very little with increasing, reversible shear
729 load.

730 From this analysis, we conclude that the stress state alone does not fully determine the
731 hydraulic transport capacity of a rock fracture. It seems that there is an interplay between fracture
732 geometry and the state of stress (shear and normal stress applied on the fracture) that determines
733 fracture transmissivity. To examine the exact contribution of shear stress applied on the fracture,
734 more complex elastic-plastic models are required. First attempts going in this direction are the
735 models of Yastrebov et al. (2017) and those of Shvarts and Yastrebov (2018a, ;2018b) where the
736 problem is approached through spectral boundary element methods. These methods should
737 allow, in term, the extension to shear stress and plasticity (Frerot et al., 2019) with the
738 geometries used in this study (grooves sub-orthogonal to fluid flow and shear sense as well as
739 parallel ones).



740

741 Figure 13. The contribution of reversible shear stress to fault transmissivity. All panels show
 742 Transmissivity vs. effective stress applied on the fracture. Full colored lines represent the
 743 exponential fit from the calibrated numerical models of transmissivity in faults submitted only to
 744 normal stress. The shaded areas represent the estimated error associated to the model. Circles
 745 represent the measured value of transmissivity under both normal and shear stress. Vertical lines
 746 show the difference between the two values at the experimental measured normal stress at the
 747 onset of reactivation. The vertical lines show therefore the contribution of shear stress to
 748 transmissivity. panels a; b; c; and d represent the samples M_{LO} ; M_{SO} ; M_f ; and M_{LP} respectively.
 749 Darker and lighter colors represent experiments conducted at 20 and 10 MPa effective
 750 confinement pressure respectively.

751

752 The effect of (irreversible) shear displacement.

753

Once that irreversible shear displacement started and the fault reached a ‘steady state’

754

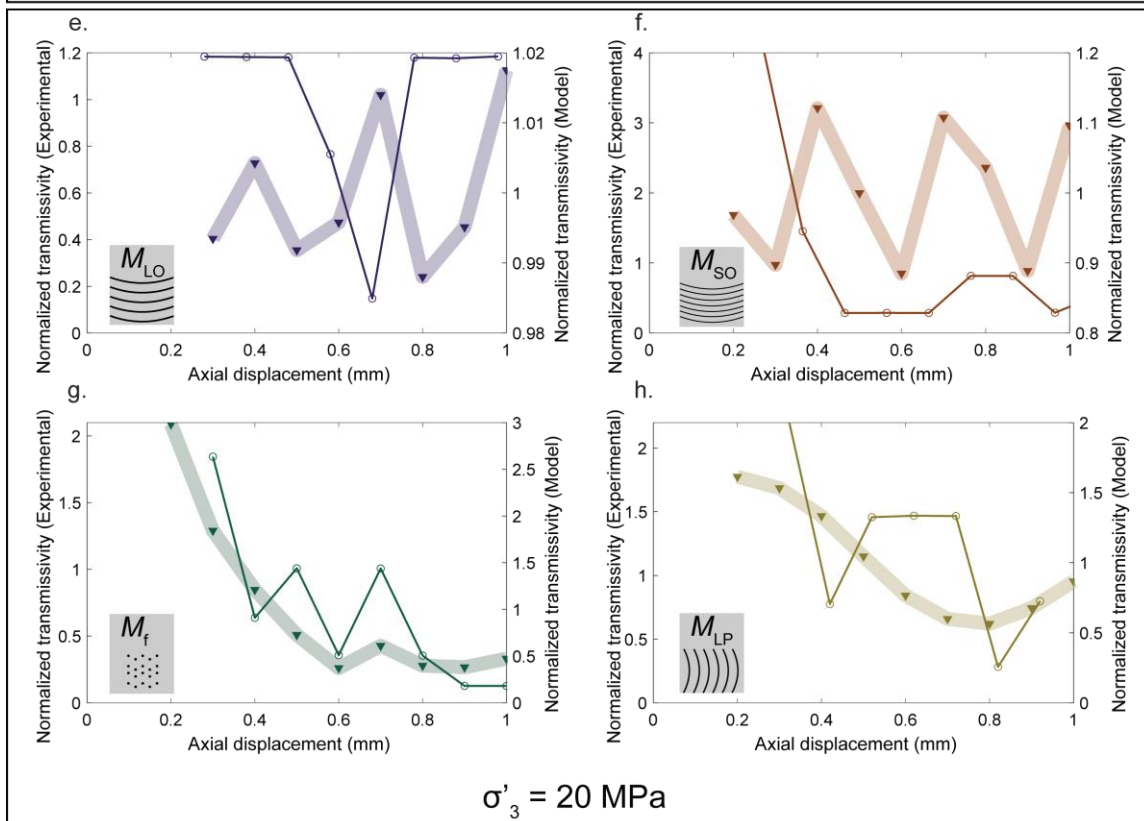
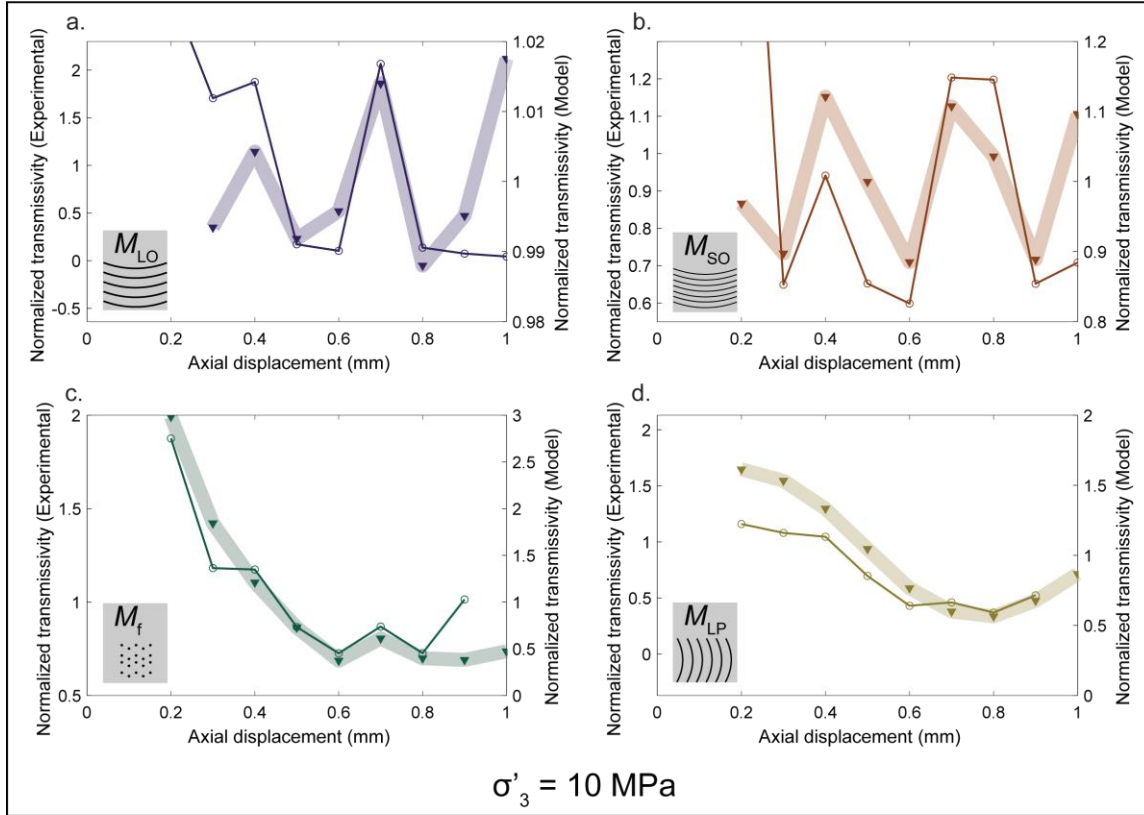
sliding condition, with near constant shear and normal stresses, the fault’s transmissivity varied

755 only slightly, usually of less than one order of magnitude (Figure 6). Our experimental results of
756 change in transmissivity during shear sliding are plotted as full lines (with empty circles as
757 markers, left y-axes) in Figure 14. There, transmissivity is normalized by the mean fracture
758 transmissivity during shear sliding.

759 In order to isolate the effect of increasing shear displacement from the effect of normal
760 loading on fracture's transmissivity (through the use of the numerical model), the shear problem
761 is simplified. To do it, the wavy rough surfaces are simply shifted of a given displacement, and
762 then the normal loading and fluid flow models are applied (See section 3.3 for details; and Figure
763 4d) with no shear loading nor wear components. In this case, the applied load on the shifted
764 fracture surfaces corresponds to the mean experimentally measured normal stress during shear
765 sliding ($\sigma'_{N_{SS}}$ in Table 1). The numerical results from the model are plotted as thick transparent
766 areas (with filled triangles as markers, right y-axes) in Figure 14. Again, the values are
767 normalized by the mean fracture transmissivity during shear sliding. On the one hand, in
768 experiments conducted at low confining pressure ($\sigma'_3 = 10$ MPa; Figure 14a-d), the general
769 tendency of transmissivity change is fairly well captured by the simplified model even though
770 the absolute values can be off by more than an order of magnitude. On the other hand, at high
771 confining pressures ($\sigma'_3 = 20$ MPa; Figure 14e-h), the simplified model is far from capturing the
772 tendency of transmissivity change with ongoing shear slip. We interpret these differences at low
773 and high confining pressure as due to strong changes in surface roughness (due to plastic
774 deformation and wear) with ongoing slip. Indeed, the model presented here is extremely
775 simplified because it does neither consider the evolution of an applied shear stress on the
776 fracture's macroscopic wavelengths nor the production of wear particles (Aghababaei et al.,
777 2016; Milanese et al., 2019; Molinari et al., 2018). The plasticity (Frerot et al., 2019) and wear
778 (Archard., 1953; Molinari et al., 2018) processes should be enhanced by higher applied normal
779 and shear stresses, thus generating larger changes in surface topography in our experiments at
780 high confining pressures. In turn, the generation of a third body during frictional sliding is
781 expected to highly contribute to i) the frictional sliding process (a review is given in Scholz,
782 2019) and ii) the fracture transmissivity (Faoro et al., 2009; Tanikawa et al., 2010; Rutter and
783 Mecklenburgh., 2017; 2018).

784 We note that, a more refined model should consider not only the deformations due to
785 shear stress (Park and Song, 2013) but mostly to wear processes and the formation of a third
786 body (Aghababaei et al., 2017; Milanese et al., 2019; Molinari et al., 2018).

787



789 Figure 14. Transmissivity change during irreversible shear displacement. All transmissivity
790 values are normalized by the mean transmissivity during shear to show the change with
791 increasing displacement. Empty circles (full lines) represent experimental results and full
792 triangles (transparent lines) represent numerical results described in section 6.2. a-d. Experiments
793 at 10 MPa effective stress the simplified model captures the overall evolution of transmissivity
794 with ongoing displacement. e-h. Experiments at 20 MPa effective stress. At high normal stress,
795 the simplified model fails to capture the transmissivity change.

796

797 After shearing, the axial stress on all samples was decreased (i.e both normal and shear
798 stress were decreased to isostatic loading conditions) and transmissivities measured again under
799 isostatic stress conditions ($\sigma'_1 = \sigma'_3$). The transmissivities after unloading (kt_{unl}) slightly
800 increased with respect to the values measured at the end of the shearing stage (last points in
801 Figure 6). Nevertheless, the transmissivity was far from being recovered to the isostatic initial
802 transmissivity. The difference between kt_0 and kt_{unl} was usually more than an order of
803 magnitude, meaning that after shearing, the faults hydraulic transport capacity was much smaller
804 even if the stress state was the same. This result can be attributed to the production of wear
805 products (thin gouge) which obstruct fluid flow in the fault, increasing the contact area and
806 reducing the hydraulic aperture at given stress conditions (Faoro et al., 2009; Tanikawa et al.,
807 2010; Rutter and Mecklenburgh, 2017, 2018). In our experiments, this is further supported by the
808 evolution of surface roughness maps after shearing (Figure 8 and Figure 9). Similar observations
809 have been made by Molecular Dynamics simulations of frictional sliding (Spijker et al., 2013)
810 where roughness decreased exponentially during sliding in hard metals. In natural faults this
811 effect is difficult to quantify. On the one hand, shear reactivation can decrease fault
812 transmissivity due to the formation of wear products at small displacements. At large
813 displacements, the wear products can become large enough that the transmissivity is in turn
814 increased depending on fault roughness and rock properties (Molinari et al., 2018; Milanese et
815 al., 2019). On the other hand, shear reactivation can increase transmissivity on ‘healed’ faults
816 (e.g. if the fault’s core is composed of glassy products and or consolidated fault gouge), due to
817 porosity unclogging (Elkhoury et al., 2011) or macroscopic dilatancy (Crawford et al., 2008;
818 Faulkner et al., 2010; Cox, 2010; Zoback and Gorelick, 2012; Jeanne et al., 2018). It is possible
819 that in faults with large scale roughness and heterogeneity, large displacements (larger than the

820 characteristic wavelength) lead to macroscopic dilation and increased fracture aperture (Chen et
821 al., 2000; Watanabe et al., 2008; 2009; Ciardo and Lecampion, 2019).

822 Further experimental work dealing with the evolution of fault roughness is needed to
823 understand how the production of wear products interacts with mechanical and hydraulic
824 aperture changes.

825 6.3 Implications for geo-energy reservoirs

826 In our experiments, the fault's transmissivity first strongly decreased due to the
827 application of normal stress, the sensitivity of fault's transmissivity to normal stress depended on
828 fracture geometry (Figure 10, 14). When shear stress was applied, its influence was very small
829 and was conditioned by the interaction between stress and fault geometries. Then, once faults
830 were submitted to shear sliding (up to 1 mm), the transmissivity changes were small (often less
831 than one order of magnitude) and its evolution could be predicted by the fault's geometry in
832 experiments at low normal stress only. During the stimulation of deep geothermal reservoirs for
833 example, one stimulation strategy to increase the production flow rate is to reactivate faults in
834 shear, expecting that the shear displacement permanently increases transmissivity (Cladouhos et
835 al., 2009; Breede et al., 2013). The strategy consists in injecting pressurized fluids into the
836 fractured reservoir in order to decrease the effective normal stress on the fault, leading to
837 reactivation. From the results in our study, we can observe that the reduction in normal stress can
838 indeed increase the fault's transmissivity and that the magnitude of increase will depend on the
839 fault surface geometry. If faults are flat but rough, the transmissivity increase will be smaller
840 than if faults present some kind of macroscopic wavelength and heterogeneous topography
841 (Watanabe et al., 2008; 2009 present somewhat similar observations in granitic rocks). In
842 addition, decreasing the fault's effective normal stress will increase the shear-to-normal stress
843 ratio (friction coefficient), thus transmissivity should change under the effect of shear stress,
844 depending on the fault's geometry. This remains valid only if the overpressure in the reservoir is
845 somehow maintained during the stimulation and production phases, reducing the reservoir's
846 effective stress.

847 The usual idea regarding fault reactivation influence on transmissivity is that slip on rough faults
848 generates an increase in hydraulic transport on the fault (Carey et al., 2015; Gale et al., 1990;
849 Guo et al., 2013; Ishibashi et al., 2012; Lee and Cho, 2002; Yeo et al., 1998; Zambrano et al.,

850 2018; Pyrak-Nolte et al., 1987; Olsson and Brown, 1993; Esaki et al., 1999; Wenning et al.,
851 2019). Nevertheless, in most of those studies, the shear displacements were in the range of 3 to
852 20 mm and/or on faults with large roughness (Chen et al., 2000; Wenning et al., 2019). Our
853 results show that when shear slip occurred in the fault (<1 mm), transmissivity remained close to
854 constant with very slight changes, in strong contrast to the usual understanding of shear
855 reactivation described above. Very few other experimental studies have reported decrease in
856 hydraulic transport properties with shear displacement (Rutter and Mecklenburgh, 2017; 2018;
857 Faoro et al., 2009; Tankikawa et al., 2010). In deep geothermal reservoirs, stimulations that
858 generate large shear displacements are usually associated with the occurrence of large magnitude
859 seismic events. In the light of our results, inducing small shear displacements will not
860 significantly increase the reservoir's fluid transport capacity. However, if the reservoir's
861 fractures and faults are 'clogged' (due to the presence of frictional wear products or by mineral
862 precipitation), it is highly possible that shear reactivation, followed by an unclogging treatment
863 (chemical or hydraulic for example) does increase the fractures transmissivities (Elkhoury et al.,
864 2011). This should be studied in future work.

865 We can conclude that changing the state of stress will improve fluid production in a larger
866 scale than generating significant offsets in the fault (which can be technologically difficult). This
867 can be done for example through stress preconditioning (Fryer et al., 2018; 2019).

868 A novelty from our study is the ability to 'predict' the shape of transmissivity changes with
869 fault reactivation at low normal stress. Indeed, as shown in section 6.3 it seems that knowledge
870 of fault surface geometry (even though this is a difficult measure to obtain) on faults submitted to
871 small normal stresses can help estimate the shape of transmissivity change with shear
872 displacement. Further work is nevertheless needed to estimate at which stress levels this
873 prediction stops being accurate and to predict the change at high normal stress. Indeed, by
874 preconditioning the reservoir (reducing the effective stress on it; Fryer et al., 2018; 2019), the
875 predictions of transmissivity should become more accurate. We can speculate that the use of
876 more complex models that include shear stress and wear processes can strongly improve the
877 prediction of transmissivity with shear displacement (Aghababaei et al., 2017; Milanese et al.,
878 2019; Molinari et al., 2018; Frerot et al., 2019; Yastrebov et al., 2017; Shvarts and Yastrebov,
879 2018a, ;2018b; Shvarts, 2019). The results obtained for a single rough-fault could then be input

880 into Discrete Fracture Models (DFM) to evaluate the hydraulic transport in fracture networks
881 (McClure and Horne, 2013).

882 **7 Conclusions**

883 In this study, we developed an experimental technique to customize the surface roughness of
884 real-rock samples which can be representative of engineered geothermal reservoirs (and more
885 generally of underground carbonate reservoirs; Delle-Piane et al., 2015; DiPippo, 2012). The
886 resulting surfaces had a fully controlled geometry which was precisely measured and analyzed
887 using the Power Spectral Density of heights (Figures 1, 7, 8 and 9). Then, single fractures of
888 Carrara marble with customized roughness were experimentally loaded under deep reservoir
889 conditions (both under normal and shear loading) to study fluid flow through the wavy-rough
890 fractures (Figures 5 and 6).

891 A numerical procedure was developed to simulate wavy-rough contacting surfaces
892 (Section 3 and Figure 10b). It was validated with the experimental data, and it allowed for the
893 isolation of the influence of different roughness parameters on fluid flow in fractures under
894 normal loading. Under normal loading, the macroscopic geometry has a strong influence on the
895 fracture's transmissivity decay (here fitted to an exponential decay) (Figure 10). Surfaces with
896 grooves sub-orthogonal to fluid flow are more sensitive to the application of normal stress than
897 samples with grooves sub-parallel to fluid flow and with no grooves in that order (Figure 10). A
898 parametric analysis of the numerical procedure on samples with grooves sub-orthogonal to fluid
899 flow showed that changes in the Hurst exponent and in the roll-off wavevector alone have little
900 influence on transmissivity (Figure 11). On the other hand, the standard deviation of heights and
901 the macroscopic wavelength have a strong influence on hydraulic transport capacity (Figure 11).
902 The evolution of transmissivity has a strong non-monotonic dependence on these two parameters
903 (Figure 13).

904 Similar experimental fractures were loaded in shear and the numerical procedure was
905 then used to isolate the effect of reversible shear loads on the fracture transmissivity (during
906 elastic deformation, Figure 13). The influence of reversible shear load on fault's transmissivity is
907 almost negligible and that its magnitude depends on the fault's geometry, thus it is not
908 straightforward to estimate how reversible shear loading affects fracture transmissivity. Finally,
909 the effect of irreversible shear displacement on transmissivity was studied with support on the

910 numerical procedure. It is found that increasing shear displacement (until 1 mm) generally
911 decreases fracture transmissivity with slight variations at each displacement step (of 0.1 mm up
912 to 1 mm; Figure 6). In that case, the transmissivity could be roughly predicted by changing the
913 model geometry at low normal stress (Figure 13a-d) probably because wear was not too
914 prominent. On the other hand, the geometrical model is completely off when normal stress is
915 high during shear reactivation (Figure 13 e-h), probably due to prominent wear and surface
916 topography changes (Figures 8, 9).

917 From this study, we observe that the main controls on fluid flow on rough fractures are in
918 that order: 1) stress applied on the fracture (normal to the fracture plane) 2) imbrication of the
919 main wavelengths; 3) magnitude of the largest macroscopic wavelength; 4) RMS roughness; 5)
920 shear reactivation; 6) Hurst exponent and roll-off wave-vector of the power spectral density of
921 heights.

922 Further work is needed to develop a numerical procedure that allows simulating fractures
923 under both normal and shear stresses. The target model should also include examination of shear
924 induced plastic deformation and wear processes. This would allow coupling the evolution of
925 fault roughness with the hydraulic transport properties as shear reactivation occurs.

926 In the light of our results, during EGS stimulations, small shear displacements will not
927 significantly increase the reservoir's permeability (unless porosity unclogging occurs). In turn,
928 reducing the effective stress on the reservoir's fractures and faults will generate large
929 permeability increases and improve the ability to predict its evolution.

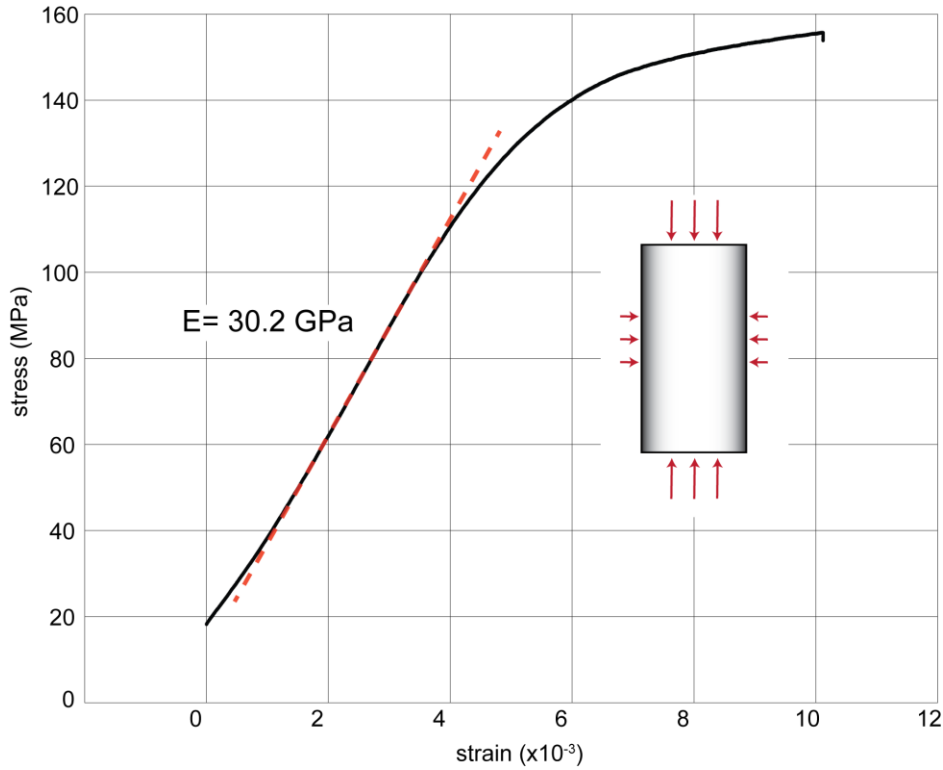
930 **Acknowledgments and Data**

931 M.A. and M.V. acknowledge the funding support from the Swiss National Science Foundation
932 (SNF), project no. PYAPP2160588, and the technical staff at LEMR for help with sample
933 preparation. M.V. acknowledges the European Research Council Starting Grant project 757290-
934 BEFINE. M.A acknowledges Francois Passelègue; Federica Paglialunga, Carolina Giorgetti, and

935 Barnaby Fryer for fruitful discussions. The authors declare no competing interests. All the data
936 related to this manuscript are being uploaded to Zenodo.org.

937 **Annex 1: Deformation of intact Carrara Marble.**

938

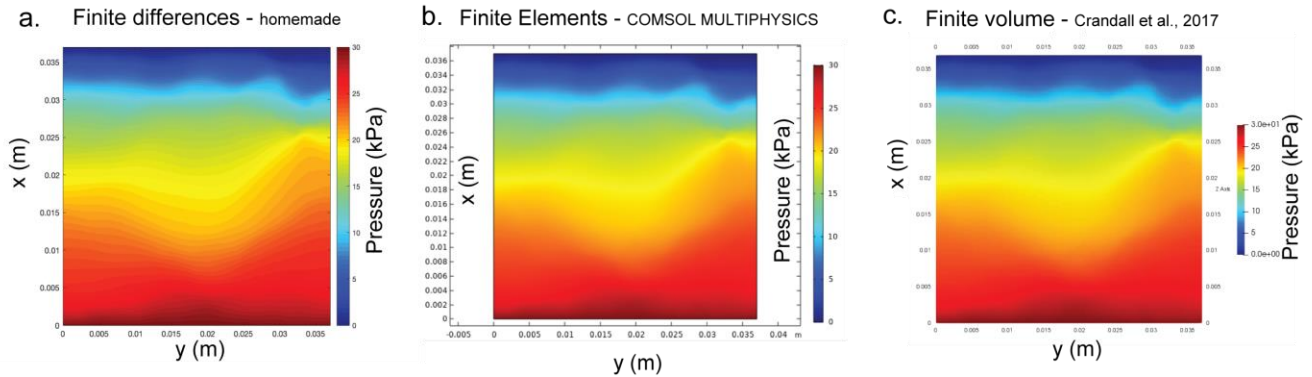


939

940 Figure A1. Experimental deformation of Carrara Marble. Differential stress versus axial strain.

941 The data was used to determine the contact model parameters ($E = 30$ GPa).

942

943 **Annex 2: Fluid flow model validation.**

944

945 Figure A2. Fluid flow model validation. Pressure distribution obtained for the flow through
 946 parallel smooth plates. Three different models were tested for solving the Reynolds boundary
 947 lubrication approximation. a. Home-made finite difference model run on Matlab. b. Finite
 948 element model run on COMSOL multiphysics. c. Finite volume model

949 **References**

950 Acosta, M., Passelègue, F.X., Schubnel, A., Madariaga, R. and Violay, M., 2019. Can precursory moment release
 951 scale with earthquake magnitude? A view from the laboratory. *Geophysical Research Letters*, 46(22), pp.12927-
 952 12937.

953

954 Acosta, M., Violay, M. 2020, Mechanical and hydraulic transport properties of transverse-isotropic Gneiss deformed
 955 under deep reservoir stress and pressure conditions. *International journal of rock mechanics and mining sciences*.

956

957 Aghababaei, R., Warner, D.H. and Molinari, J.F., 2016. Critical length scale controls adhesive wear mechanisms.
 958 *Nature communications*, 7(1), pp.1-8.

959

960 Akchurin, A., Bosman, R., Lugt, P.M. and van Drogen, M., 2015. On a model for the prediction of the friction
 961 coefficient in mixed lubrication based on a load-sharing concept with measured surface roughness. *Tribology letters*,
 962 59(1), p.19.

963

964 Almakari, M., Chauris, H., Passelègue, F. X., Dublanchet, P., Gesret, A. 2020. Fault's hydraulic diffusivity
 965 enhancement during injection induced fault reactivation: Application of pore pressure diffusion inversions to
 966 laboratory injection experiments. *Submitted*.

967

968 Bay, N. and Wanheim, T., 1976. Real area of contact and friction stress at high pressure sliding contact. *Wear*,
 969 38(2), pp.201-209.

970
971 Bayart, E., Svetlizky, I. and Fineberg, J., 2016. Fracture mechanics determine the lengths of interface ruptures that
972 mediate frictional motion. *Nature Physics*, 12(2), pp.166-170.
973
974 Ben-David, O., Rubinstein, S.M. and Fineberg, J., 2010. Slip-stick and the evolution of frictional strength. *Nature*,
975 463(7277), pp.76-79.
976
977 Bernabé, Y., Mok, U. and Evans, B., 2006. A note on the oscillating flow method for measuring rock permeability.
978 *International journal of rock mechanics and mining sciences (1997)*, 43(2), pp.311-316.
979
980 Breede, K., Dzebisashvili, K., Liu, X. and Falcone, G., 2013. A systematic review of enhanced (or engineered)
981 geothermal systems: past, present and future. *Geothermal Energy*, 1(1), p.4.
982
983 Brown, S., Caprihan, A. and Hardy, R., 1998. Experimental observation of fluid flow channels in a single fracture.
984 *Journal of Geophysical Research: Solid Earth*, 103(B3), pp.5125-5132.
985
986 Brown, S.R. and Scholz, C.H., 1985. Broad bandwidth study of the topography of natural rock surfaces. *Journal of*
987 *Geophysical Research: Solid Earth*, 90(B14), pp.12575-12582.
988
989 Brown, S.R., 1987. A note on the description of surface roughness using fractal dimension. *Geophysical Research*
990 *Letters*, 14(11), pp.1095-1098.
991
992 Brown, S.R., 1987. Fluid flow through rock joints: the effect of surface roughness. *Journal of Geophysical*
993 *Research: Solid Earth*, 92(B2), pp.1337-1347.
994
995 Brush, D.J. and Thomson, N.R., 2003. Fluid flow in synthetic rough-walled fractures: Navier-Stokes, Stokes, and
996 local cubic law simulations. *Water Resources Research*, 39(4).
997
998 Byerlee, J., 1978. Friction of rocks. In *Rock friction and earthquake prediction* (pp. 615-626). Birkhäuser, Basel.
999
1000 Byerlee, J.D. and Summers, R., 1975. Stable sliding preceding stick-slip on fault surfaces in granite at high pressure.
1001 In *Earthquake Prediction and Rock Mechanics* (pp. 63-68). Birkhäuser, Basel.
1002
1003 Candela, T., Renard, F., Bouchon, M., Brouste, A., Marsan, D., Schmittbuhl, J. and Voisin, C., 2009.
1004 Characterization of fault roughness at various scales: Implications of three-dimensional high resolution topography
1005 measurements. In *Mechanics, structure and evolution of fault zones* (pp. 1817-1851). Birkhäuser Basel.
1006

- 1007 Candela, T., Renard, F., Klinger, Y., Mair, K., Schmittbuhl, J. and Brodsky, E.E., 2012. Roughness of fault surfaces
1008 over nine decades of length scales. *Journal of Geophysical Research: Solid Earth*, 117(B8).
1009
- 1010 Carey, J.W., Lei, Z., Rougier, E., Mori, H. and Viswanathan, H., 2015. Fracture-permeability behavior of shale.
1011 *Journal of unconventional oil and gas resources*, 11, pp.27-43.
1012
- 1013 Chen, J., 1995. *Effects of deformation on compressibility and permeability of Carrara Marble* (Doctoral
1014 dissertation, Massachusetts Institute of Technology).
1015
- 1016 Chen, Z., Narayan, S.P., Yang, Z. and Rahman, S.S., 2000. An experimental investigation of hydraulic behaviour of
1017 fractures and joints in granitic rock. *International Journal of Rock Mechanics and Mining Sciences*, 37(7), pp.1061-
1018 1071.
1019
- 1020 Ciardo, F. and Lecampion, B., 2019. Effect of dilatancy on the transition from aseismic to seismic slip due to fluid
1021 injection in a fault. *Journal of Geophysical Research: Solid Earth*, 124(4), pp.3724-3743.
1022
- 1023 Cladouhos, T., Petty, S., Foulger, G., Julian, B. and Fehler, M., 2010. Injection induced seismicity and geothermal
1024 energy. *GRC Transactions*, 34, pp.1213-1220.
1025
- 1026 Cox, S.F., 2010. The application of failure mode diagrams for exploring the roles of fluid pressure and stress states
1027 in controlling styles of fracture-controlled permeability enhancement in faults and shear zones. *Geofluids*, 10(1-2),
1028 pp.217-233.
1029
- 1030 Crandall, D., Moore, J., Gill, M. and Stadelman, M., 2017. CT scanning and flow measurements of shale fractures
1031 after multiple shearing events. *International Journal of Rock Mechanics and Mining Sciences*, 100, pp.177-187.
1032
- 1033 Crawford, B.R., Faulkner, D.R. and Rutter, E.H., 2008. Strength, porosity, and permeability development during
1034 hydrostatic and shear loading of synthetic quartz-clay fault gouge. *Journal of Geophysical Research: Solid Earth*,
1035 113(B3).
1036
- 1037 Delle Piane, C., Arena, A., Sarout, J., Esteban, L. and Cazes, E., 2015. Micro-crack enhanced permeability in tight
1038 rocks: An experimental and microstructural study. *Tectonophysics*, 665, pp.149-156.
1039
- 1040 Dieterich, J.H. and Kilgore, B.D., 1994. Direct observation of frictional contacts: New insights for state-dependent
1041 properties. *Pure and Applied Geophysics*, 143(1-3), pp.283-302.
1042

- 1043 Dieterich, J.H., 1979. Modeling of rock friction: 1. Experimental results and constitutive equations. *Journal of*
1044 *Geophysical Research: Solid Earth*, 84(B5), pp.2161-2168.
- 1045
- 1046 DiPippo, R., 2012. *Geothermal power plants: principles, applications, case studies and environmental impact.*
1047 Butterworth-Heinemann.
- 1048
- 1049 Edmond, J. M., and M. S. Paterson. "Volume changes during the deformation of rocks at high pressures." In
1050 *International Journal of Rock Mechanics and Mining Sciences and Geomechanics Abstracts*, vol. 9, no. 2, pp. 161-
1051 182. Pergamon, 1972.
- 1052
- 1053 Elkhoury, J.E., Niemeijer, A., Brodsky, E.E. and Marone, C., 2011. Laboratory observations of permeability
1054 enhancement by fluid pressure oscillation of in situ fractured rock. *Journal of Geophysical Research: Solid Earth*,
1055 116(B2).
- 1056
- 1057 Ellsworth, W.L., 2013. Injection-induced earthquakes. *Science*, 341(6142), p.1225942.
- 1058
- 1059 Esaki, T., Du, S., Mitani, Y., Ikusada, K. and Jing, L., 1999. Development of a shear-flow test apparatus and
1060 determination of coupled properties for a single rock joint. *International Journal of Rock Mechanics and Mining*
1061 *Sciences*, 36(5), pp.641-650.
- 1062
- 1063 Faoro, I., Niemeijer, A., Marone, C. and Elsworth, D., 2009. Influence of shear and deviatoric stress on the
1064 evolution of permeability in fractured rock. *Journal of Geophysical Research: Solid Earth*, 114(B1).
- 1065
- 1066 Faulkner, D.R., Jackson, C.A.L., Lunn, R.J., Schlische, R.W., Shipton, Z.K., Wibberley, C.A.J. and Withjack, M.O.,
1067 2010. A review of recent developments concerning the structure, mechanics and fluid flow properties of fault zones.
1068 *Journal of Structural Geology*, 32(11), pp.1557-1575.
- 1069
- 1070 Frérot, L., Bonnet, M., Molinari, J.F. and Anciaux, G., 2019. A Fourier-accelerated volume integral method for
1071 elastoplastic contact. *Computer Methods in Applied Mechanics and Engineering*, 351, pp.951-976.
- 1072
- 1073 Fryer, B., Siddiqi, G. and Laloui, L., 2018. Reservoir Stimulation's Effect on Depletion-Induced Seismicity. *Journal*
1074 *of Geophysical Research: Solid Earth*, 123(9), pp.7806-7823.
- 1075
- 1076 Fryer, B., Siddiqi, G. and Laloui, L., 2020. Injection-induced seismicity: strategies for reducing risk using high
1077 stress path reservoirs and temperature-induced stress preconditioning. *Geophysical Journal International*, 220(2),
1078 pp.1436-1446.
- 1079

- 1080 Goebel, T.H. and Brodsky, E.E., 2018. The spatial footprint of injection wells in a global compilation of induced
1081 earthquake sequences. *Science*, 361(6405), pp.899-904.
- 1082
- 1083 Grasselli, G. and Egger, P., 2003. Constitutive law for the shear strength of rock joints based on three-dimensional
1084 surface parameters. *International Journal of Rock Mechanics and Mining Sciences*, 40(1), pp.25-40.
- 1085
- 1086 Grigoli, F., Cesca, S., Priolo, E., Rinaldi, A.P., Clinton, J.F., Stabile, T.A., Dost, B., Fernandez, M.G., Wiemer, S.
1087 and Dahm, T., 2017. Current challenges in monitoring, discrimination, and management of induced seismicity
1088 related to underground industrial activities: A European perspective. *Reviews of Geophysics*, 55(2), pp.310-340.
- 1089
- 1090 Guo, T., Zhang, S., Gao, J., Zhang, J. and Yu, H., 2013. Experimental study of fracture permeability for stimulated
1091 reservoir volume (SRV) in shale formation. *Transport in porous media*, 98(3), pp.525-542.
- 1092
- 1093 Hakami, E., 1989. *Water flow in single rock joints* (No. STRIPA-TR--89-08). Swedish Nuclear Fuel and Waste
1094 Management Co..
- 1095
- 1096 Ishibashi, T., Watanabe, N., Hirano, N., Okamoto, A. and Tsuchiya, N., 2012. Upgrading of aperture model based
1097 on surface geometry of natural fracture for evaluating channeling flow. *Geothermal Resources Council,
1098 Transactions*, 36, pp.481-486.
- 1099
- 1100 Iwai, K., 1976. Fundamental studies of fluid flow through a single fracture. *Ph. D. thesis, Univ. of California*.
- 1101
- 1102 Jacobs, T.D., Junge, T. and Pastewka, L., 2017. Quantitative characterization of surface topography using spectral
1103 analysis. *Surface Topography: Metrology and Properties*, 5(1), p.013001.
- 1104
- 1105 Jaeger, J.C., Cook, N.G. and Zimmerman, R., 2009. *Fundamentals of rock mechanics*. John Wiley and Sons.
- 1106
- 1107 Jeanne, P., Guglielmi, Y., Rutqvist, J., Nussbaum, C. and Birkholzer, J., 2018. Permeability variations associated
1108 with fault reactivation in a claystone formation investigated by field experiments and numerical simulations. *Journal
1109 of Geophysical Research: Solid Earth*, 123(2), pp.1694-1710.
- 1110
- 1111 Kanafi, M., M., 2019. Radially averaged surface roughness/topography power spectrum (PSD)
1112 ([https://www.mathworks.com/matlabcentral/fileexchange/54297-radially-averaged-surface-roughness-topography-
1113 power-spectrum-psd](https://www.mathworks.com/matlabcentral/fileexchange/54297-radially-averaged-surface-roughness-topography-power-spectrum-psd)), MATLAB Central File Exchange. Retrieved February 23, 2019.
- 1114
- 1115 Kim, K.H., Ree, J.H., Kim, Y., Kim, S., Kang, S.Y. and Seo, W., 2018. Assessing whether the 2017 Mw 5.4 Pohang
1116 earthquake in South Korea was an induced event. *Science*, 360(6392), pp.1007-1009.

- 1117
- 1118 Konzuk, J.S. and Kueper, B.H., 2004. Evaluation of cubic law based models describing single-phase flow through a
1119 rough-walled fracture. *Water Resources Research*, 40(2).
- 1120
- 1121 Lee, H.S. and Cho, T.F., 2002. Hydraulic characteristics of rough fractures in linear flow under normal and shear
1122 load. *Rock Mechanics and Rock Engineering*, 35(4), pp.299-318.
- 1123
- 1124 Lengliné, O., Lamourette, L., Vivin, L., Cuenot, N. and Schmittbuhl, J., 2014. Fluid-induced earthquakes with
1125 variable stress drop. *Journal of Geophysical Research: Solid Earth*, 119(12), pp.8900-8913.
- 1126
- 1127 Lomize, G.M., 1951. Flow in fractured rocks. *Gosenergoizdat, Moscow*, 127, p.197.
- 1128
- 1129 Lubrecht, A.A. and Ioannides, E., 1991. A fast solution of the dry contact problem and the associated sub-surface
1130 stress field, using multilevel techniques.
- 1131
- 1132 M., M., Kanafi (2018). Surface generator: artificial randomly rough surfaces
1133 ([https://www.mathworks.com/matlabcentral/fileexchange/60817-surface-generator-artificial-randomly-rough-](https://www.mathworks.com/matlabcentral/fileexchange/60817-surface-generator-artificial-randomly-rough-surfaces)
1134 [surfaces](https://www.mathworks.com/matlabcentral/fileexchange/60817-surface-generator-artificial-randomly-rough-surfaces)), MATLAB Central File Exchange. Retrieved February 23, 2018.
- 1135
- 1136 Means, W.D., 1987. A newly recognized type of slickenside striation. *Journal of Structural geology*, 9(5-6), pp.585-
1137 590.
- 1138
- 1139 Milanese, E., Brink, T., Aghababaei, R. and Molinari, J.F., 2019. Emergence of self-affine surfaces during adhesive
1140 wear. *Nature communications*, 10(1), pp.1-9.
- 1141
- 1142 Molinari, J.F., Aghababaei, R., Brink, T., Frérot, L. and Milanese, E., 2018. Adhesive wear mechanisms uncovered
1143 by atomistic simulations. *Friction*, 6(3), pp.245-259.
- 1144
- 1145 Noël, C., Pimienta, L. and Violay, M., 2019. Time-dependent deformations of sandstone during pore fluid pressure
1146 oscillations: Implications for natural and induced seismicity. *Journal of Geophysical Research: Solid Earth*, 124(1),
1147 pp.801-821.
- 1148
- 1149 Ohnaka, M., 2013. *The physics of rock failure and earthquakes*. Cambridge University Press.
- 1150
- 1151 Olsson, W.A. and Brown, S.R., 1993, December. Hydromechanical response of a fracture undergoing compression
1152 and shear. In *International journal of rock mechanics and mining sciences and geomechanics abstracts* (Vol. 30,
1153 No. 7, pp. 845-851). Pergamon.

- 1154
- 1155 Oron, A.P. and Berkowitz, B., 1998. Flow in rock fractures: The local cubic law assumption reexamined. *Water*
1156 *Resources Research*, 34(11), pp.2811-2825.
- 1157
- 1158 Park, J.W. and Song, J.J., 2013. Numerical method for the determination of contact areas of a rock joint under
1159 normal and shear loads. *International Journal of Rock Mechanics and Mining Sciences*, 58, pp.8-22.
- 1160
- 1161 Passelègue, F. X., Almakari, M., Dublanchet, P., Barras, F., Violay, M. 2020. On the nature of Earthquakes: from
1162 the field to the lab. *Submitted*.
- 1163
- 1164 Paterson, M.S. and Wong, T.F., 2005. *Experimental rock deformation-the brittle field*. Springer Science and
1165 Business Media.
- 1166
- 1167 Patir, N. and Cheng, H.S., 1978. An average flow model for determining effects of three-dimensional roughness on
1168 partial hydrodynamic lubrication.
- 1169
- 1170 Petit, J.P., 1987. Criteria for the sense of movement on fault surfaces in brittle rocks. *Journal of structural Geology*,
1171 9(5-6), pp.597-608.
- 1172
- 1173 Pieri, M., Burlini, L., Kunze, K., Stretton, I. and Olgaard, D.L., 2001. Rheological and microstructural evolution of
1174 Carrara Marble with high shear strain: results from high temperature torsion experiments. *Journal of Structural*
1175 *Geology*, 23(9), pp.1393-1413.
- 1176
- 1177 Piggott, A.R. and Elsworth, D., 1992. Analytical models for flow through obstructed domains. *Journal of*
1178 *Geophysical Research: Solid Earth*, 97(B2), pp.2085-2093.
- 1179
- 1180 Pingel, T.J., Clarke, K.C. and McBride, W.A., 2013. An improved simple morphological filter for the terrain
1181 classification of airborne LIDAR data. *ISPRS Journal of Photogrammetry and Remote Sensing*, 77, pp.21-30.
- 1182
- 1183 Polonsky, I.A. and Keer, L.M., 1999. A numerical method for solving rough contact problems based on the multi-
1184 level multi-summation and conjugate gradient techniques. *Wear*, 231(2), pp.206-219.
- 1185
- 1186 Power, W.L., Tullis, T.E., Brown, S.R., Boitnott, G.N. and Scholz, C.H., 1987. Roughness of natural fault surfaces.
1187 *Geophysical Research Letters*, 14(1), pp.29-32.
- 1188 Power, W.L. and Tullis, T.E., 1989. The relationship between slickenside surfaces in fine-grained quartz and the
1189 seismic cycle. *Journal of Structural Geology*, 11(7), pp.879-893.
- 1190

- 1191
- 1192 Pyrak-Nolte, L.J. and Morris, J.P., 2000. Single fractures under normal stress: The relation between fracture specific
1193 stiffness and fluid flow. *International Journal of Rock Mechanics and Mining Sciences*, 37(1-2), pp.245-262.
1194
- 1195 Pyrak-Nolte, L.J., Cook, N.G. and Nolte, D.D., 1988. Fluid percolation through single fractures. *Geophysical*
1196 *Research Letters*, 15(11), pp.1247-1250.
1197
- 1198 Renard, F., Candela, T. and Bouchaud, E., 2013. Constant dimensionality of fault roughness from the scale of
1199 micro-fractures to the scale of continents. *Geophysical Research Letters*, 40(1), pp.83-87.
1200
- 1201 Renshaw, C.E., 1995. On the relationship between mechanical and hydraulic apertures in rough-walled fractures.
1202 *Journal of Geophysical Research: Solid Earth*, 100(B12), pp.24629-24636.
1203
- 1204 Reynolds, Osborne. "IV. On the theory of lubrication and its application to Mr. Beauchamp tower's experiments,
1205 including an experimental determination of the viscosity of olive oil." *Philosophical transactions of the Royal*
1206 *Society of London* 177 (1886): 157-234.
1207
- 1208 Rutter, E.H. and Mecklenburgh, J., 2017. Hydraulic conductivity of bedding-parallel cracks in shale as a function of
1209 shear and normal stress. *Geological Society, London, Special Publications*, 454(1), pp.67-84.
1210
- 1211 Rutter, E.H. and Mecklenburgh, J., 2018. Influence of normal and shear stress on the hydraulic transmissivity of thin
1212 cracks in a tight quartz sandstone, a granite, and a shale. *Journal of Geophysical Research: Solid Earth*, 123(2),
1213 pp.1262-1285.
1214
- 1215 Sahli, R., Pallares, G., Ducottet, C., Ali, I.B., Al Akhrass, S., Guibert, M. and Scheibert, J., 2018. Evolution of real
1216 contact area under shear and the value of static friction of soft materials. *Proceedings of the National Academy of*
1217 *Sciences*, 115(3), pp.471-476.
1218
- 1219 Scholz, C., Molnar, P. and Johnson, T., 1972. Detailed studies of frictional sliding of granite and implications for the
1220 earthquake mechanism. *Journal of geophysical research*, 77(32), pp.6392-6406.
1221
- 1222 Shvarts, A., 2019. *Coupling mechanical frictional contact with interfacial fluid flow at small and large scales*
1223 (Doctoral dissertation).
1224
- 1225 Shvarts, A.G. and Yastrebov, V.A., 2018a. Trapped fluid in contact interface. *Journal of the Mechanics and Physics*
1226 *of Solids*, 119, pp.140-162.
1227

- 1228 Shvarts, A.G. and Yastrebov, V.A., 2018b. Fluid flow across a wavy channel brought in contact. *Tribology*
1229 *International*, 126, pp.116-126.
1230
- 1231 Sibson, R.H., 1994. Crustal stress, faulting and fluid flow. *Geological Society, London, Special Publications*, 78(1),
1232 pp.69-84.
1233
- 1234 Sibson, R.H., 1996. Structural permeability of fluid-driven fault-fracture meshes. *Journal of Structural Geology*,
1235 18(8), pp.1031-1042.
- 1236 Spijker, P., Anciaux, G. and Molinari, J.F., 2013. Relations between roughness, temperature and dry sliding friction
1237 at the atomic scale. *Tribology International*, 59, pp.222-229.
1238
- 1239 Svetlizky, I. and Fineberg, J., 2014. Classical shear cracks drive the onset of dry frictional motion. *Nature*,
1240 509(7499), pp.205-208.
1241
- 1242 Tanikawa, W., Sakaguchi, M., Tadai, O. and Hirose, T., 2010. Influence of fault slip rate on shear-induced
1243 permeability. *Journal of Geophysical Research: Solid Earth*, 115(B7).
1244
- 1245 Tembe, S., Lockner, D.A. and Wong, T.F., 2010. Effect of clay content and mineralogy on frictional sliding
1246 behavior of simulated gouges: Binary and ternary mixtures of quartz, illite, and montmorillonite. *Journal of*
1247 *Geophysical Research: Solid Earth*, 115(B3).
1248
- 1249 Townend, J. and Zoback, M.D., 2000. How faulting keeps the crust strong. *Geology*, 28(5), pp.399-402.
1250
- 1251 Toy, V.G., Niemeijer, A., Renard, F., Morales, L. and Wirth, R., 2017. Striation and slickenline development on
1252 quartz fault surfaces at crustal conditions: Origin and effect on friction. *Journal of Geophysical Research: Solid*
1253 *Earth*, 122(5), pp.3497-3512.
1254
- 1255 Violay, M., Nielsen, S., Gibert, B., Spagnuolo, E., Cavallo, A., Azais, P., Vinciguerra, S. and Di Toro, G., 2014.
1256 Effect of water on the frictional behavior of cohesive rocks during earthquakes. *Geology*, 42(1), pp.27-30.
1257
- 1258 Violay, M., Gibert, B., Mainprice, D. and Burg, J.P., 2015. Brittle versus ductile deformation as the main control of
1259 the deep fluid circulation in oceanic crust. *Geophysical Research Letters*, 42(8), pp.2767-2773.
1260
- 1261 Violay, M., Heap, M.J., Acosta, M. and Madonna, C., 2017. Porosity evolution at the brittle-ductile transition in the
1262 continental crust: Implications for deep hydro-geothermal circulation. *Scientific reports*, 7(1), pp.1-10.
1263

- 1264 Walsh, J.B. and Brace, W.F., 1984. The effect of pressure on porosity and the transport properties of rock. *Journal*
1265 *of Geophysical Research: Solid Earth*, 89(B11), pp.9425-9431.
1266
- 1267 Walsh, J.B., 1981, Effect of pore pressure and confining pressure on fracture permeability. In *International Journal*
1268 *of Rock Mechanics and Mining Sciences and Geomechanics Abstracts* (Vol. 18, No. 5, pp. 429-435). Pergamon.
1269
- 1270 Watanabe, N., Hirano, N. and Tsuchiya, N., 2008. Determination of aperture structure and fluid flow in a rock
1271 fracture by high-resolution numerical modeling on the basis of a flow-through experiment under confining pressure.
1272 *Water Resources Research*, 44(6).
1273
- 1274 Watanabe, N., Hirano, N. and Tsuchiya, N., 2009. Diversity of channeling flow in heterogeneous aperture
1275 distribution inferred from integrated experimental-numerical analysis on flow through shear fracture in granite.
1276 *Journal of Geophysical Research: Solid Earth*, 114(B4).
1277
- 1278 Weber, B., Suhina, T., Brouwer, A.M. and Bonn, D., 2019. Frictional weakening of slip interfaces. *Science*
1279 *advances*, 5(4), p.eaav7603.
1280
- 1281 Wenning, Q.C., Madonna, C., Kurotori, T. and Pini, R., 2019. Spatial mapping of fracture aperture changes with
1282 shear displacement using X-ray computerized tomography.
1283
- 1284 Witherspoon, P.A., Wang, J.S., Iwai, K. and Gale, J.E., 1980. Validity of cubic law for fluid flow in a deformable
1285 rock fracture. *Water resources research*, 16(6), pp.1016-1024.
1286
- 1287 Yastrebov, V.A., Anciaux, G. and Molinari, J.F., 2017. The role of the roughness spectral breadth in elastic contact
1288 of rough surfaces. *Journal of the Mechanics and Physics of Solids*, 107, pp.469-493.
1289
- 1290 Yeck, W.L., Weingarten, M., Benz, H.M., McNamara, D.E., Bergman, E.A., Herrmann, R.B., Rubinstein, J.L. and
1291 Earle, P.S., 2016. Far-field pressurization likely caused one of the largest injection induced earthquakes by
1292 reactivating a large preexisting basement fault structure. *Geophysical Research Letters*, 43(19), pp.10-198.
1293
- 1294 Yeo, I.W., De Freitas, M.H. and Zimmerman, R.W., 1998. Effect of shear displacement on the aperture and
1295 permeability of a rock fracture. *International Journal of Rock Mechanics and Mining Sciences*, 35(8), pp.1051-1070.
1296
- 1297 Zambrano, M., Tondi, E., Mancini, L., Lanzafame, G., Trias, F.X., Arzilli, F., Materazzi, M. and Torrieri, S., 2018.
1298 Fluid flow simulation and permeability computation in deformed porous carbonate grainstones. *Advances in water*
1299 *resources*, 115, pp.95-111.
1300

1301 Zbinden, D., Rinaldi, A.P., Diehl, T. and Wiemer, S., 2019. Potential influence of overpressurized gas on the
1302 induced seismicity in the St. Gallen deep geothermal project (Switzerland): Gallen deep geothermal project
1303 (Switzerland). *Solid Earth Discussions*.

1304

1305 Zhang, S., Cox, S.F. and Paterson, M.S., 1994. The influence of room temperature deformation on porosity and
1306 permeability in calcite aggregates. *Journal of Geophysical Research: Solid Earth*, 99(B8), pp.15761-15775.

1307

1308 Zimmerman, R.W. and Bodvarsson, G.S., 1996. Hydraulic conductivity of rock fractures. *Transport in porous*
1309 *media*, 23(1), pp.1-30.

1310

1311 Zoback, Mark D., and Steven M. Gorelick. "Earthquake triggering and large-scale geologic storage of carbon
1312 dioxide." *Proceedings of the National Academy of Sciences* 109, no. 26 (2012): 10164-10168.

1313